Thermal and Thermoelectric Properties of Nanostructured Materials and Interfaces

Hao-Hsiang Liao

Dissertation submitted to the faculty of the Virginia Polytechnic Institute and State University in partial fulfillment of the requirements for the degree of

Doctor of Philosophy
In
Mechanical Engineering

Scott T. Huxtable, Chair
Thomas E. Diller
Kathleen Meehan
Giti Khodaparast
Mark R. Paul

November 27, 2012
Blacksburg, VA

Keywords: Nanoscale heat transport, time-domain thermoreflectance, thermoelectric, nanocrystalline alloys, bulk metallic glasses

Thermal and Thermoelectric Properties of Nanostructured Materials and Interfaces

Hao-Hsiang Liao

Abstract

Many modern technologies are enabled by the use of thin films and/or nanostructured composite materials. For example, many thermoelectric devices, solar cells, power electronics, thermal barrier coatings, and hard disk drives contain nanostructured materials where the thermal conductivity of the material is a critical parameter for the device performance. At the nanoscale, the mean free path and wavelength of heat carriers may become comparable to or smaller than the size of a nanostructured material and/or device. For nanostructured materials made from semiconductors and insulators, the additional phonon scattering mechanisms associated with the high density of interfaces and boundaries introduces additional resistances that can significantly change the thermal conductivity of the material as compared to a macroscale counterpart. Thus, better understanding and control of nanoscale heat conduction in solids is important scientifically and for the engineering applications mentioned above.

In this dissertation, I discuss my work in two areas dealing with nanoscale thermal transport: (1) I describe my development and advancement of important thermal characterization tools for measurements of thermal and thermoelectric properties of a variety of materials from thin films to nanostructured bulk systems, and (2) I discuss my measurements on several materials systems done with these characterization tools.

First, I describe the development, assembly, and modification of a time-domain thermoreflectance (TDTR) system that we use to measure the thermal conductivity and

the interface thermal conductance of a variety of samples including nanocrystalline alloys of Ni-Fe and Co-P, bulk metallic glasses, and other thin films. Next, a unique thermoelectric measurement system was designed and assembled for measurements of electrical resistivity and thermopower of thermoelectric materials in the temperature range of 20 to 350 °C. Finally, a commercial Anter Flashline 3000 thermal diffusivity measurement system is used to measure the thermal diffusivitiy and heat capacity of bulk materials at high temperatures.

With regards to the specific experiments, I examine the thermal conductivity and interface thermal conductance of two different types of nanocrystalline metallic alloys of nickel-iron and cobalt-phosphorus. I find that the thermal conductivity of the nanocrystalline alloys is reduced by a factor of approximately two from the thermal conductivity measured on metallic alloys with larger grain sizes. With subsequent molecular dynamics simulations performed by a collaborator, and my own electrical conductivity measurements, we determine that this strong reduction in thermal conductivity is the result of increased electron scattering at the grain boundaries, and that the phonon component of the thermal conductivity is largely unchanged by the grain boundaries.

We also examine four complex bulk metallic glass (BMG) materials with compositions of $Zr_{50}Cu_{40}Al_{10}$, $Cu_{46.25}Zr_{44.25}Al_{7.5}Er_2$, $Fe_{48}Cr_{15}Mo_{14}C_{15}B_6Er_2$, and $Ti_{41.5}Zr_{2.5}Hf_5Cu_{42.5}Ni_{7.5}Si_1$. From these measurements, I find that the addition of even a small percentage of heavy atoms (i.e. Hf and Er) into complex disordered BMG structures can create a significant reduction in the phonon thermal conductivity of these

materials. This work also indicates that the addition of these heavy atoms does not disrupt electron transport to the degree with which thermal transport is reduced.

Dedications

To my parents and my wife

Acknowledgements

First of all, I would like to express my sincere gratitude to my PhD advisor, Prof. Scott Huxtable. Personally, Prof. Huxtable is a very nice and humble person. Academically, he gives research opportunities for students to explore and guides students intelligently and patiently. He is apparently not only a respectful advisor but also a great mentor over the years. As being an international student in the United States, I greatly appreciate his support, encouragement and guidance along with my graduate studies.

Second, I would like to thank my committee member, Prof. Giti Khodaparast, in the Department of Physics. At the beginning of my graduate studies, she was very kind to allow us to use the laser and equipment in her lab. I learned a great deal about laser physics and optics from her. She always smiles and encourages me every time we meet. Also, I would like to thank my other committee members, Prof. Thomas Diller, Prof. Kathleen Meehan and Prof. Mark Paul for advising me in my graduate studies.

Third, I would like to thank Prof. Peter Liaw in the Department of Materials Science & Engineering at University of Tennessee-Knoxville (UT-K). Prof. Liaw was my advisor for my undergraduate studies at UT-K. After I left, he was still very supportive and he was always willing to provide any assistance I needed.

I also would like to thank Prof. William Reynolds and Prof. Mitsuhiro Murayama in the Department of Materials Science & Engineering. I greatly appreciate the assistance and guidance they gave me at the Nanoscale Characterization and Fabrication Laboratory. Specifically, they taught me how to cut polish samples, they helped with electron microscopy, and I learned a considerable amount about material analysis and sample characterization.

I also would like to thank many friends from Virginia Tech, Knoxville, and elsewhere. I am thankful for my many friends and colleagues who assisted me with my research work: Nitin Shukla, Harikrishna, Chris Vernieri, Ganesh Balasubramanian, William Wu, Teyu Chien, Krishna Vummidi, Jue Wang, Yu (Grace) Zhang & her husband (Mingkai Mu), Wenli Zhang, Donald Leber, Gongyao Wang, Fengxiao Liu, Wei Wu, Jianfei Zhang, and others. I am also thankful for many friends: Peter Lin & his wife (Wendy Tsai), Sam Wang & his wife (Rona), Zhenzhen Zhang, Pei-Yin (Vivian) Ho, Chia-Liang Tsai & his wife (Wan-Ting Wang), Apoorva Shende, Saurabh Bisht, Sai Sreedharan, Saugata Sarkar, Weiwei Hu, Ya Wang, and others.

Finally, I would like to thank my family including my parents (Mei-Chiang Liao and Shu-Chih Chen) in Taiwan and my wife (Yuling Lin). Without their spiritual support, care and patience, I could not go this far for my education.

Table of Contents

List of Figures

List of Tables

1. Introduction

1.1. Heat transfer methods

Heat transfer occurs in three modes: conduction, convection, and radiation. Heat conduction dominates for thermal transport through solids, heat convection is important for liquids and gases, and radiation is significant at high temperatures and/or vacuum conditions. In this dissertation, my work focuses on heat conduction in nanostructured solid materials and through solid-solid interfaces.

1.2. Size effects in heat transport phenomena

Thermal energy in solids is carried by electrons and quantized lattice vibrations called phonons. These heat carriers behave differently at the nanoscale as the mean free path (mfp) and/or wavelength of carriers becomes comparable to, or smaller than, the size of the nanostructure. These size effects in heat transport phenomena become important at the nanoscale and nanostructured materials may have vastly different thermal properties than their bulk counterparts. Size effects in heat conduction are briefly discussed below in two size-regimes: macroscale and nanoscale heat conduction.

1.2.1. Macroscale heat conduction

For structures with dimensions one micrometer and larger, the lengthscales are much larger than the mean free path and/or wavelength of heat carriers. Thus, these dimensions are considered to be macroscale, where heat conduction in solids can be accurately described through Fourier's law of heat conduction. Fourier's law states that the heat flux $q_x^{"}$ is proportional to the temperature gradient:

$$q_x'' = -k \cdot dT/dx \tag{1.1}$$

where the proportionality constant, k, is the thermal conductivity of the solid, T is temperature, and x is direction of heat transfer. The negative sign indicates that heat always flows from hot to cold. The thermal conductivity, k, indicates the efficiency with which a material conducts heat.

At the macroscale, the density of interfaces and boundaries is low, thus interface thermal resistance is generally small compared to the resistance of the bulk material. One specific exception is for interfaces between materials that are not in intimate contact. For example, interfaces between nominally flat solids where the interface roughness may be on the order of microns or larger, can have non-negligible interface resistance. For materials with roughness on this scale, the actual area of contact may only be on the order of a few percent of the nominal contact area. Thus, the thermal conductance of these interfaces is controlled primarily by the area of contact between the two materials. In this dissertation, I examine materials in intimate contact, i.e. cases where there is complete contact between the two materials.

1.2.2. Nanoscale heat conduction

While Fourier's law accurately describes heat transport at the macroscale, it also obscures the underlying fundamental mechanisms that govern heat conduction [1-4]. In order to understand and describe thermal transport at the nanoscale, one must look closely at how thermal energy propagates through materials and across interfaces between materials. As mentioned previously, two different carriers control heat conduction: (a) electrons and (b) quantized lattice vibrations called phonons. Thus, k consists of an electronic component, k_e and a phonon (or lattice) component, k_p, i.e. $k = k_e$

+ k_p. Typically, materials that are good conductors of heat, such as metals, are also efficient carriers of heat due to the electronic component of the thermal conductivity. For electrically insulating materials, thermal conductivity is controlled by the phonon component. Insulating materials can have excellent thermal conductivity, e.g. diamond, if they are made of defect free lattices with strong and stiff bonds. On the other hand, if the insulating material is amorphous, e.g. glass or polymer, thermal conductivity is low since the disorganized lattice with little long-range order disrupts the phonons. Semiconductors, naturally, fall in between metals and insulators, and either the electronic or lattice components may dominate depending on the doping within the material.

While electrons are likely a familiar concept to most, phonons may not be as familiar. Lattice vibrations can be pictured by considering an atom to be a small mass, and the bond between adjacent atoms as a spring. Thus, phonons are analogous to vibrational energy that is transmitted along a spring-mass system. The lattice spacing, masses, and spring constants determine the allowed (quantized) vibrations.

The mean free path (mfp) of an electron or phonon in a material can be defined as the average distance the carrier travels before it collides with another carrier, impurity, interface, grain boundary, etc. At room temperature, the mfp for electrons is typically on the order of 10 nm, while the mfp for phonons is generally around 10-100 nm, depending on the material. Thus, when the characteristic lengthscale of the material of interest is much larger than the mean free path, i.e. ~ one micrometer, heat conduction is in the macroscale regime and Fourier's law holds. However, for lengthscales less than approximately one micrometer, the size of the system influences the allowed lattice vibrations and the effects of boundaries, surfaces, and interfaces begin to dominate. Thus

heat conduction at the micro and nanoscale can be very different from macroscale behavior, and this nanoscale behavior is frequently non-intuitive.

A better understanding of nanoscale heat transfer would impact a variety of technologies, as engineers now have the ability to design and fabricate numerous devices with critical lengthscales below 100 nm. For example, many power electronic devices, thermal barrier coatings, magnetic actuators, thermoelectric (TE) devices, etc., are made of nanostructured materials, and in all of these technologies nanoscale thermal transport plays a critical role in device performance. My work mainly focuses on examining thermal properties of nanostructured materials including nanostructured TE materials for waste heat recovery in vehicles, which is described in the next paragraph.

1.3. Nanostructured materials for thermoelectric applications

A thermoelectric material may be used to either (a) convert a temperature gradient into electrical power, or (b) use electrical energy into generate a thermal gradient [5-11]. In all heat engines a large fraction of energy is rejected as waste heat, thus there are opportunities for thermoelectric devices to capture some of this otherwise wasted energy, and convert that energy into useful work. For example, roughly 30% of the chemical energy in gasoline and diesel engines is wasted as hot exhaust gas [12]. With improvements in efficiency, thermoelectric devices could convert some of the energy in the hot exhaust gas in vehicles into useful electrical work that could then be used to improve fuel economy and to reduce harmful exhaust emissions [13-15]. Our goals in this thermoelectric project are to create devices with 1) high TE conversion efficiency 2) long-term reliability 3) manufacturability at high volume and low cost.

The efficiency of a TE material can be quantified with the dimensionless figure of merit:

$$ZT = S^2\sigma T/k \tag{1.2}$$

where S is the Seebeck coefficient, σ is the electrical conductivity, k is the thermal conductivity, and T is absolute temperature. In order for thermoelectric devices to gain widespread use and acceptance in the automotive and other industries, materials with enhanced *ZT* are required. Improving *ZT* has remained a significant challenge for decades as the Seebeck coefficient and electrical and thermal conductivities are all related. Methods to increase the Seebeck coefficient have the undesirable effect of also reducing electrical conductivity and vice-versa. Similarly, many techniques for reducing thermal conductivity also hinder electrical transport [16]. However, the use of nanostructured materials has recently been shown to be a promising approach for the reduction of thermal conductivity with minimal corresponding reduction in electrical conductivity. If these nanostructured materials are properly scaled, the numerous interfaces may increase phonon scattering and reduce thermal conductivity, yet leave electrons largely unperturbed. Thus, in order to improve the efficiency of thermoelectric devices, it is critical to understand heat transfer in these nanostructured materials [17-23].

The most efficient commercially available thermoelectric material is bismuth telluride (Bi_2Te_3) with a *ZT* ~1 near room temperature. Poudel et al. [24] have created a nanocrystalline P-type bismuth antimony telluride bulk alloy with a significant reduction in thermal conductivity, which enhances its *ZT* to ~1.4 at 100 °C. However, ZT for bismuth telluride decreases at the higher temperatures that are useful for power generation from waste heat. Moreover, bismuth telluride and its counterpart for higher

temperature power generation lead telluride (like many other thermoelectric materials) are either expensive, of limited supply, and/or toxic [25].

Our TE materials will be fabricated from materials in the silicide and skutterudite families and provided by our collaborator, Prof. Pryia's group, in the Dept. of Materials Science & Engineering at Virginia Tech. For our automotive power generation applications, we are interested in the temperature range of 100 to 350 °C. My contribution to our thermoelectric work is in the measurements and understanding of the thermoelectric properties of these new materials at these elevated temperatures. Specifically, I designed and built an automated thermoelectric measurement system as described in Chapter 3 for thermoelectric property measurements from room temperature up to 350 °C.

1.4. Nanocrystalline alloys and bulk metallic glasses (BMGs)

In addition to the thermoelectric materials, we are also interested in examining thermal properties of some other bulk nanocrystalline and amorphous alloys as these materials are important for other technologies, and they also give valuable insight into general heat transfer trends in nanostructured composites. In my research, we have examined a variety of materials such as nanocrystalline nickel-iron (Ni-18%Fe) and cobalt-phosphorus (Co-1.65%P) materials, as well as bulk metallic glasses (BMGs). Ni-Fe alloys are selected as the materials of interest because of their relatively low thermal expansion coefficient and favorable magnetic properties, which makes them strong candidates for applications such as thermostatic bimetals, glass sealants, electronic packages, and magnetic actuators [26-30]. We have investigated the electronic and phonon contributions to the thermal conductivity of a nanocrystalline Ni-18%Fe alloy

using a combination of fundamental molecular simulations and experimental measurements to predict the influence of varying composition on the thermal transport through the material.

BMGs are well-known for their great strength, hardness, toughness, corrosion and resistance which are promising for various applications such as sporting goods, bicycle frames, corrosion resistance materials, machine tools, etc. [31] We have experimentally measured the electron and phonon contributions to thermal conductivity for four different BMGs at room temperature.

This document includes six chapters. Additional background related to nanoscale heat transfer and the materials we examine is given in Chapter 2. The three primary experimental techniques developed and used in this work are described in Chapter 3. Chapters 4 and 5 detail the results on two different projects dealing with thermal transport in metallic alloys (Ni-Fe and Co-P), and in a variety of bulk metallic glasses, respectively. Chapter 6 briefly reviews my contributions to other research projects that I have worked on at Virginia Tech. Finally, a summary of this work and suggestions for future work appear in Chapter 7.

2. Background

In this chapter, the nanocrystalline and thermoelectric materials are introduced, and the heat transport mechanisms in bulk materials are examined.

2.1. Nanocrystalline materials

In 1989, Gleiter [32] used the term "nanocrystalline materials" for a new group of disordered materials which typically have a grain size of 100 nm or less. Due to this structure, these materials have properties that may differ greatly from similar coarse-grained materials. Gleiter also stated that these materials have the common microstructural feature that consists of a high density of interfacial defects. Figure 1 shows the atomic structure in a two-dimensional nanocrystalline material where the black circles represent atoms in the centers of the crystals, and the open circles indicate atoms in the intercrystalline region. Nanocrystalline materials are synthesized by a variety of techniques, and the grain size can be tuned by synthesizing parameters. Since the grain sizes of nanocrystalline materials are small, there is a large volume fraction of intercrystalline components like grain boundaries and interfaces existing in those materials. Depending on their dimensionalities, there are four classifications of structures as shown in Figure 2: zero-dimensional (atom clusters, i.e. quantum dots), one-dimensional (multilayers, i.e. quantum wires), two-dimensional (overlayers, i.e. quantum wells) and three-dimensional nanostructures (equiaxed nanostructures, i.e. bulk semiconductors) [29, 33].

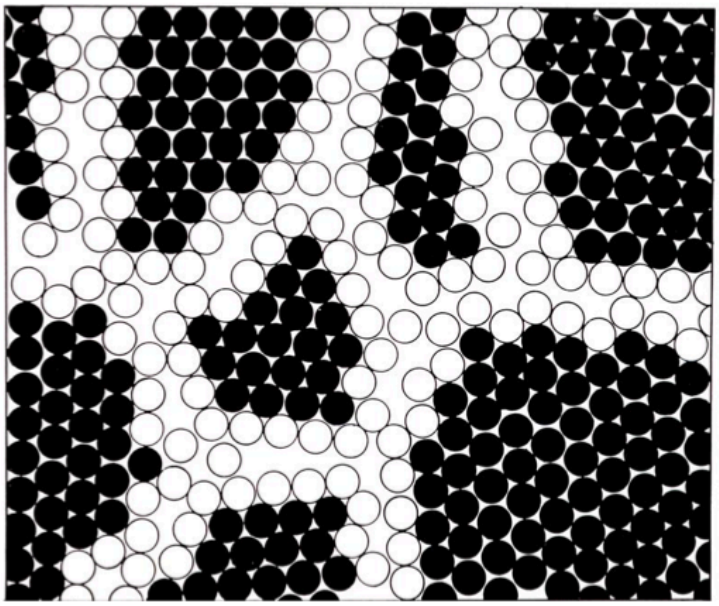

Figure 1: An atomic structure of a two-dimensional nanocrystalline material where atoms are located in the crystalline (closed circle) and intercrystalline (open circle) regions. (image from Gleiter [32])

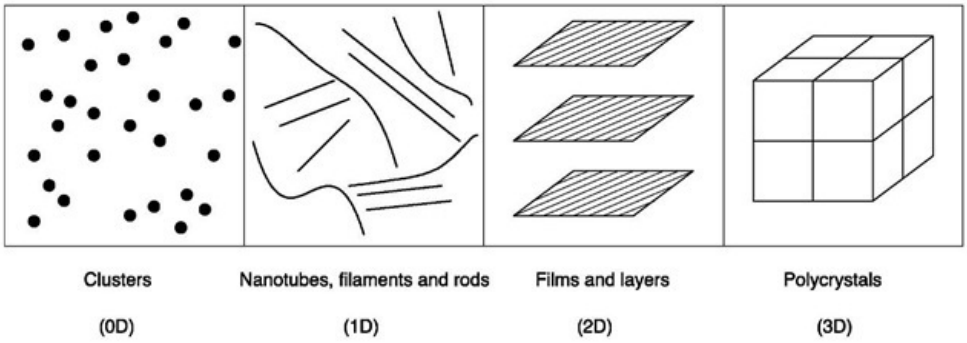

Figure 2: Types of nanocrystalline materials: zero-dimensional, one-dimensional, two-dimensional and three dimensional (image from Nanocrystalline Materials: Synthesis and Properties Part 1[34]).

2.2. Structure sensitivity and grain size dependence

Polycrystalline materials and alloys have been widely studied for a long time. In 2010, Erb [35] reviewed the grain size dependence of various properties for nanocrystalline electroformed nickel as shown here in Table 1. Additionally, Erb

summarized the structure sensitivities of polycrystalline materials in Table 2 from the classical materials text book by A. L. Ruoff [36]. By comparing Table 1 with Table 2, one can observe that there are no major changes for the most of properties. However, the thermal conductivity for nanocrystalline alloys remains uncertain. In one of my research topics, the thermal conductivity of nanocrystalline Ni-Fe and Co-P alloys are examined and discussed in Chapter 4.

Table 1: Grain size dependences of various properties for nanocrystalline electroformed nickel (table from Erb [35])

Strong Grain Size Dependence	**Weak Grain Size Dependence**
Hardness	Young's modulus
Yield Strength	Fatigue Performance
Tensile Strength	Thermal Expansion
Elongation to Fracture	Specific Heat
Coefficient of Friction	Saturation magnetization
Abrasive Wear Resistance	Curie Temperature
Adhesive Wear Resistance	Salt Spray Corrosion Resistance
Localized Corrosion	Passivity in Corrosion
Hydrogen Diffusivity	
Electrical Resistivity	
Coercivity	

Table 2: Structure sensitivities in conventional polycrystalline materials (table from Erb [35] summarized from Ruoff [36])

Property	**Structure-Insensitive**	**Structure-Sensitive**
Mechanical	Density Elastic moduli	Mechanical loss angle Tensile yield stress Fracture strength Plasticity
Thermal	Thermal expansion (at high temperatures) Melting point Specific heat (at high temperatures) Heat of fusion	Thermal conductivity (at low temperatures)
Electrical	Resistivity (metallic) at high temperatures Dielectric constant Saturation polarization of ferroelectric materials	Resistivity in semiconductors and metals (at low temperatures) Electrical loss angle
Magnetic	Paramagnetic and diamagnetic properties Saturation induction of ferromagnetic materials	Ferromagnetic properties (including magnetostriction) except saturation induction
Superconductive	Transition temperature	Current carrying capacity

2.3. Heat conduction in nanostructured materials by phonons

At the macroscale, Fourier's law accurately describes heat conduction. However, as device geometries shrink to beyond sub-micron lengthscales, the mean free path of heat carriers (i.e. phonons and/or electrons) becomes comparable or larger than the critical feature size of the material. In nanoscale heat conduction, the additional scattering mechanisms introduced by the high density of interfaces and boundaries inside the medium become dominate over the bulk thermal resistance of the material. In this

chapter, we focus on the fundamental understanding of phonon effects in heat conduction.

2.3.1. Phonon mean free path

As described earlier in Chapter 1, phonons are quantized lattice vibrations, and phonons are the dominant carrier of thermal energy in semiconductors and electrical insulators. Based on kinetic theory, the phonon mean free path, l, can be expressed:

$$l = {}^{3k}/_{Cv} \tag{2.1}$$

where k is the thermal conductivity, C is the specific heat per volume and v is the speed of sound. The phonon mfp can be limited by various scattering mechanisms such as phonon-phonon scattering, phonon-impurity scattering and phonon-boundary scattering [37, 38]. Equation 2.1 is a general expression for phonon mean free path that assumes that all phonons have the same energy and velocity.

2.3.2. Phonon scattering

In solids, there are two types of phonon scattering [39]: elastic phonon scattering and inelastic phonon scattering. In elastic phonon scattering, phonons are scattered by lattice imperfections such as defects, impurities, grain boundaries or dislocations where the phonon frequency remains the same. However, in inelastic phonon scattering, three or more phonons are involved and the phonon frequency changes.

Phonon scattering is the dominant form of thermal resistance for heat conduction in non-metallic solids. The difference between phonon scattering at the macroscale as compared with the nanoscale is that at the nanoscale additional scattering mechanisms are introduced due to size effects. For example, superlattices are periodic structures typically composed of alternating thin layers of two different materials. In these multilayer

structures where the thickness of each layer may be less than the phonon mfp and/or wavelength, the thermal boundary resistance dominates the thermal conductivity of the superlattice [40-42]. It has been shown in many cases that, due to the thermal boundary resistance, superlattices may exhibit thermal conductivities far below that of either of the constituent materials. However, the thermal behavior of these nanostructured materials is not only a simple function of the additional thermal boundary resistance between the layers. In 1997, Lee and Cahill measured the thermal conductivity of Si-Ge superlattices with superlattice period (L) over a range of 30-275 Å. They found that for short periods, $30<L<70$ Å, the thermal conductivity of the superlattice decreases with decreasing L as shown in Figure 3. Since shorter periods give a higher density of interfaces per unit length, this result could be expected. However, at longer periods with L above 100 Å, even smaller thermal conductivity values were observed. This counterintuitive result was likely due to increased defects associated with strain-induced defects and dislocations between the silicon and germanium layers due to the large lattice mismatch (~4%) between Si and Ge. This trend underscores the difficulty in interpreting measurements of thermal transport in nanostructures as one also needs corresponding structural measurements on the sample as well.

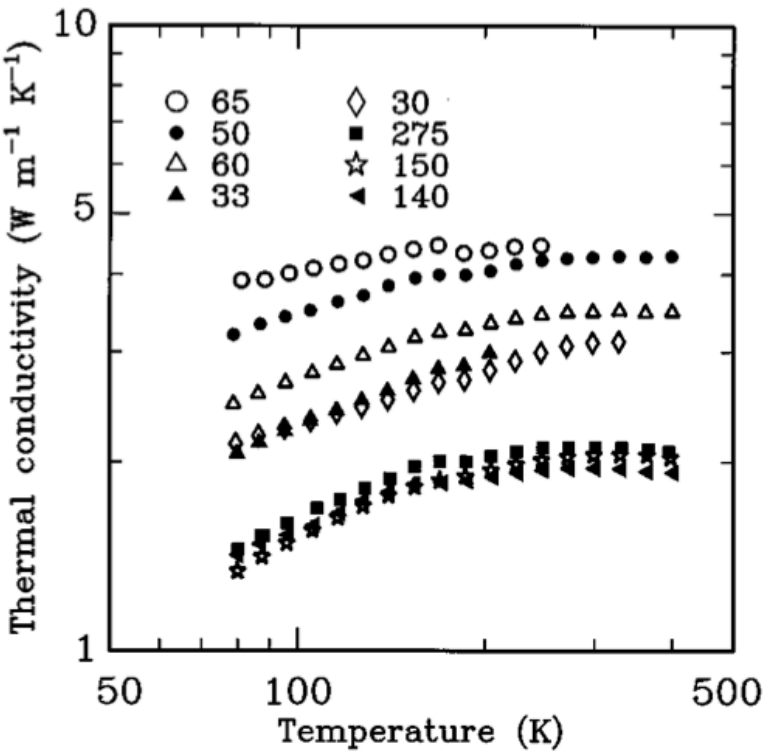

Figure 3: Thermal conductivity of Si-Ge superlattices. The label on each symbol is corresponds to the superlattice period *L* measured in Å (image from Lee [42]).

2.3.2.1. Elastic phonon scattering

As described previously, elastic phonon scattering events due to lattice imperfections such as dislocations, defects, and boundaries due not change the frequency of the incident phonon. Figure 4 shows a perfect one-dimensional spring-mass system representing atoms in crystal that are connected with each other through chemical bounds. A phonon is a quantized lattice vibration in a crystal so we can treat those imperfections as a spring-mass system with unsystematic masses and/or spring stiffness.

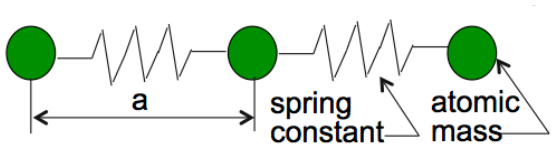

Figure 4: A one-dimensional spring-mass system where atoms are represented by point masses in a solid crystal that are held by chemical bounds (springs). The letter *a* represents the lattice constant or the lattice parameter.

Another explanation of elastic phonon scattering involves the use of the acoustic impedance, Z, of a material. The acoustic impedance of a material for phonons is analogous to the index of refraction for electromagnetic waves. The acoustic impedance is defined as

$$Z = \rho v \tag{2.2}$$

where ρ is the mass density and v is the speed of sound in the material. The speed of sound is defined as

$$v = \sqrt{\frac{C}{\rho}} \tag{2.3}$$

where C is the elastic stiffness of the chemical bonds. From Equation (2.2) & (2.3), the acoustic impedance can be determined directly from knowledge of the mass density and chemical bonds. In a crystal, lattice imperfections will not have the same atomic mass or spring stiffness as the rest of the system. Due to this change in mass and/or spring constant, phonons will scatter, just as photons do when they encounter a change in refractive index.

2.3.2.2. Inelastic phonon scattering

Inelastic phonon scattering occurs when phonons are scattered by interacting with other phonons. This type of scattering often occurs due to anharmonicity in the interatomic forces. This anharmonicity is the result of the lattice vibrations deforming the

bond (spring) beyond its elastic range causing the stiffness to change. So as one phonon encounters a different spring constant, the phonon may scatter.

There are two types of inelastic phonon scattering processes [39]: "normal" and "Umklapp" scattering processes. Figure 5(a) represents the normal scattering process: two phonons (wave vectors, K_1 and K_2) combined to create a third phonon (wave vector, K_3) while Figure 5(b) also represents the normal scattering process: a single phonon (wave vector, K_1) is split into two phonons (wave vectors, K_2 and K_3). For the normal scattering process, the phonon momentum and energy are conserved. This conservation requires:

$$\omega_1 + \omega_2 = \omega_3 \ \& \ \overrightarrow{K_1} + \overrightarrow{K_2} = \overrightarrow{K_3} \text{ for the case in Figure 5(a)} \quad (2.4)$$

$$\omega_1 = \omega_2 + \omega_3 \ \& \ \overrightarrow{K_1} = \overrightarrow{K_2} + \overrightarrow{K_3} \text{ for the case in Figure 5(b)} \quad (2.5)$$

Since the energy and momentum are conserved, the normal process does not produce any direct resistance to heat flow. However, since normal processes alter the phonon frequencies, then can indirectly contribute to thermal resistance by making other scattering processes more likely.

On the other hand, for Umklapp process, the phonon momentum is not conserved, and this is more important for thermal conductivity. Figure 5(c) is a schematic diagram showing the Umklapp scattering process that requires:

$$\omega_1 + \omega_2 = \omega_3 \ \& \ \overrightarrow{K_1} + \overrightarrow{K_2} = \overrightarrow{K_3} + \vec{G} \text{ for the case in Figure 5(c)} \quad (2.6)$$

where $\vec{G}$ is called the reciprocal wave vector. In Figure 5(c), similar to the normal scattering process, the two phonons (wave vectors, K_1 and K_2) combine in an attempt to produce a third phonon (wave vectors, K_3). However, due to the discrete nature of the atomic lattice, the summations of the two wave vectors ($\overrightarrow{K_1} + \overrightarrow{K_2}$) may exceed the

maximum limit of the first Brillouin zone ($K = \pi/a$) where a is the spacing between atoms. Since the wavelength of a crystal cannot be smaller than $2a$, it is not possible to produce a phonon with a vector greater than π/a. Thus, when the summations $\left(\overrightarrow{K_1} + \overrightarrow{K_2}\right)$ is greater than π/a, a third reciprocal wave vector, $\vec{G}$, must be added as shown in Equation (2.6) [39, 43]. Unlike the normal scattering process, the Umklapp scattering process produces direct resistance to the heat flow, and this mechanism dominates thermal conductivity in semiconductors and insulators at room temperature.

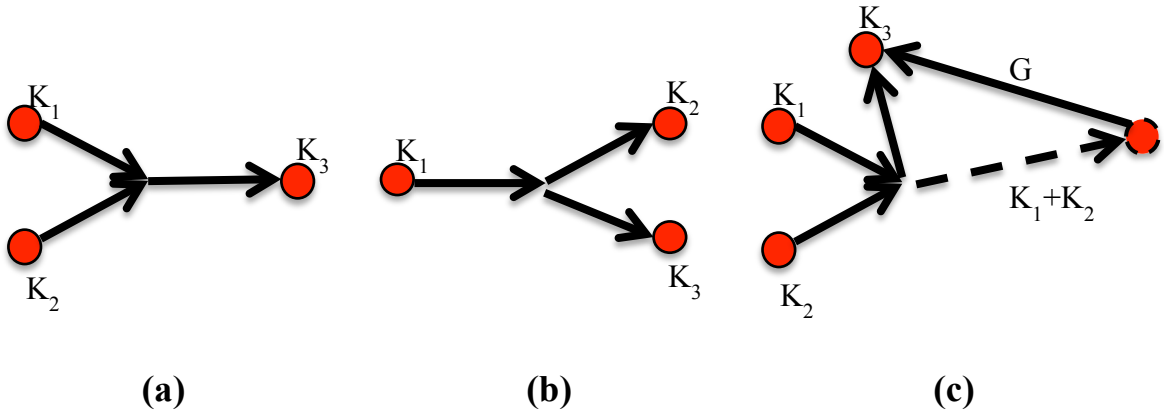

Figure 5: Inelastic phonon scattering processes: (a) Normal scattering process (b) Normal scattering process (c) Umklapp scattering process.

2.4. Reduction of thermal conductivity for thermoelectric applications

As described above, phonon scattering could become an adjustable parameter in order to selectively tune the thermal conductivity in nanostructured materials. For my work with thermoelectric materials, we are interested in reducing thermal conductivity without causing a corresponding reduction in electrical conductivity, as this would increase the efficiency of the TE material as shown in Equation 1.2. Due to the rich

variety of phonon scattering mechanisms, and the ability to fabricate and characterize materials at the nanoscale, the use of structure and size-effects become an interesting avenue for improving thermoelectric materials. Research into the use of nanostructured and low-dimensional materials for thermoelectrics took off about 20 years ago after Hicks and Dresselhaus [22, 44] showed theoretically that quantum confinement in nanostructured materials could lead to a large increase the Seebeck coefficient without a reduction in electrical conductivity. While realizing these potential gains in Seebeck coefficient have proven to be difficult, the intense interest and work on nanoscale thermoelectric materials has resulted in significant gains through the reduction of thermal conductivity in these materials [11, 45, 46].

3. Experimental Techniques

3.1. Time-domain Thermoreflectance (TDTR)

The thermal conductivity, k, is measured using time-domain thermoreflectance (TDTR) [47-50]. TDTR is a pump-probe optical technique that can be used to simultaneously extract thermal conductivity for a material and interface thermal conductance between two layers. This technique takes advantage of the fact that the reflectivity of a metal depends slightly on temperature.

A Mira Optima 900-F ultrafast titanium:sapphire laser from Coherent Inc. is used for our TDTR system. The Mira is pumped with a 10-Watt Verdi V10 laser also from Coherent. The Verdi output beam of 532 nm is sent to the titanium:sapphire crystal in the Mira to produce a mode-locked ultrafast laser pulse (~100 fs pulsewidth) with a repetition rate of 76 MHz. Figure 6 shows a schematic diagram of the optical path of my TDTR system. The 780 nm wavelength output beam from the Mira is split into two beams called the "pump" and "probe" beams with a 50:50 beam splitter. The pump beam is used to heat the surface of a sample, and the time-delayed probe beam is used to measure the temperature-induced change in reflectivity at the sample surface. The thermal conductivity and interface thermal conductance are extracted simultaneously by comparing the experimental data to theoretical model.

After the laser beam passes through the beam splitter, we use one 500 mm lens and one Keplerian telescope system on the pump-beam path in order to control the diameter of the beam. Similarly, there are two Keplerian telescope systems on the probe-beam path. The reason for the different lens systems is to control both beam diameters independently. The probe beam diameter is more difficult to control since that beam has a

variable pathlength due to the delay stage. In addition, there are several neutral density filters on both pump- and probe- paths to adjust the beam power, which are not shown in Figure 6.

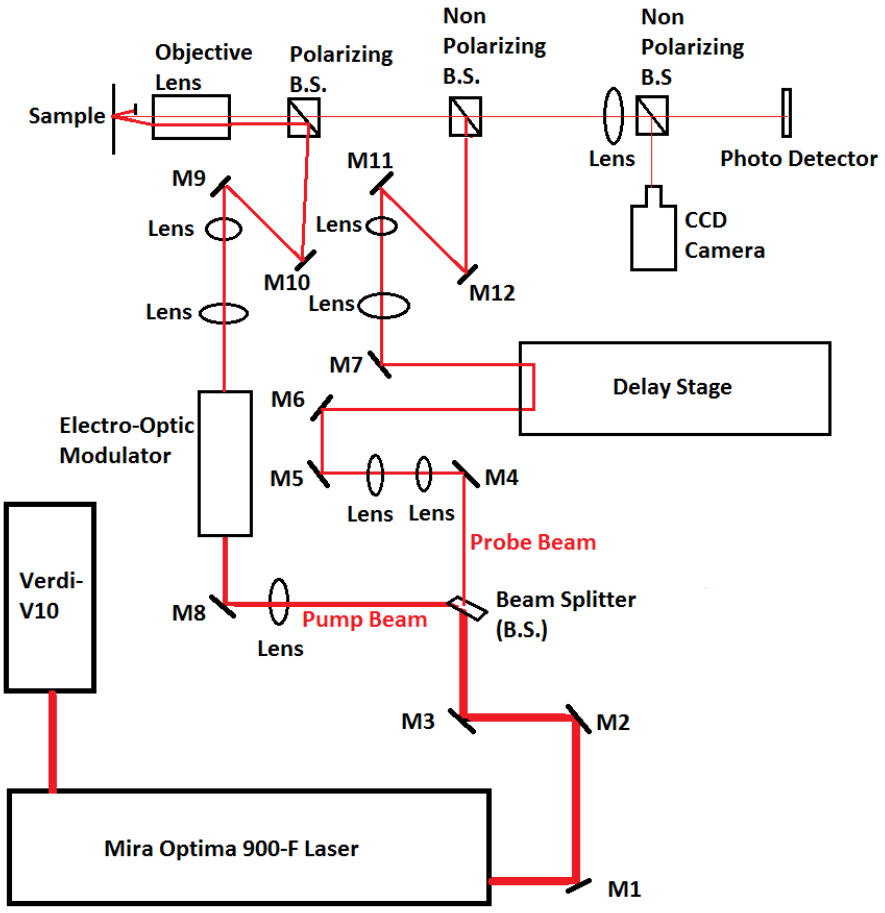

Figure 6: Schematic diagram of the optical path of the time-domain thermoreflectance (TDTR) system using a Verdi and Mira system from Coherent. A 10-Watt pump Verdi V10 laser beam is sent to a titanium:sapphire crystal in the Mira to produce a mode-locked ultrafast laser pulse with a repetition rate of 76 MHz. The 780 nm wavelength output is split into pump and probe beams with a 50:50 beam splitter after the third mirror (M3). The pump beam is modulated at ~10 MHz by the electro-optic modulator and is focused on the sample with the objective lens. The arrival time of the probe beam at the

sample is controlled with the mechanical delay stage. There are four lens systems in total to adjust the pump and probe beam diameters. The pump and probe beams are focused by objective lens and they are focus on the same spot on the sample. The sample image can be viewed on the screen by using CCD camera. By measuring the thermally induced change in reflectivity of the probe beam with the photodetector and lock-in amplifier we get a measure of how the sample temperature changes as a function of time. With the use of a thermal model in conjunction with our experimental data, we can extract the thermal conductivity and interface thermal conductance of our samples.

The pump beam passes an electro-optic modulator (E.O.M.) and is modulated at a frequency in a range of ~10 MHz. The pump beam is then directed to the sample with a polarizing beam splitter and a standard microscope objective lens. The energy in the pump beam is absorbed within the first 15 nm of the aluminum film, thus it provides nearly an ideal periodic heat source at the surface of the sample. After the pump beam heats the sample, there is nearly instantaneous (~3 ps) temperature rise on the sample surface, and the heat diffuses into the sample. The arrival time of the probe beam at the sample is controlled by a mechanical delay stage, and the probe beam is used to monitor the change in reflectivity at the sample surface. As mentioned earlier, the reflectivity of the aluminum has a measurable dependence on temperature, dR/dT, in the near infrared. In fact, aluminum has one of the largest dR/dT values among metals in the IR at room temperature ($dR/dT \sim 2 \times 10^{-4}$ K^{-1} at a wavelength of 780 nm) [51]. Since aluminum is inexpensive, easy to evaporate, and has good adhesion with a wide range of materials, it is an excellent choice for TDTR measurements.

By monitoring the reflectivity of the aluminum film we can measure the thermal decay at the sample surface. The rate at which the aluminum cools is, of course, a function of the thermal resistance of the layer(s) below the aluminum. This change in reflectivity of the probe beam is monitored with a photodiode detector, and the output from the photodiode is measured with a lock-in amplifier (Stanford Research Systems

model 844). The lock-in amplifier records the in-phase (V_{in}) and out-of-phase (V_{out}) components of the voltage from the photodiode. The use of the lock-in and the in-phase and out-of-phase voltage greatly improves the signal-to-noise ratio in our measurements. We ultimately use the ratio of the two voltages ($-V_{in}/V_{out}$) in order to reduce experimental noise as many errors in the measurement system (such as defocusing of the probe beam due to the delay stage travel) affect the in-phase and out-of-phase voltages in the same manner. Thus, by using the ratio of the voltages, these errors cancel.

Sample experimental data from TDTR measurements are shown in Figure 7. In this figure we see a jump in the in-phase (V_{in}) signal at t=0 which corresponds to the time when the pump and probe beams arrive at the sample simultaneously. This rapid increase in V_{in} shows that the energy in the pump beam is absorbed within 2-3 ps. The out-of-phase signal (V_{out}) should remain nearly constant across t=0. This feature is useful when setting the phase of the lock-in. Also of interest in these data at short delay times is the appearance of an acoustic echo around t=35 ps. When the laser energy is absorbed at the surface of the sample, the lattice expands rapidly and a sound wave propagates through the aluminum. This sound wave is partially reflected at the interface between the aluminum and the sample, and when the wave returns to the surface the reflectivity changes due to the strain at the surface. Since the speed of sound in aluminum is known to be 6420 m/s (or nm/ps), we can accurately determine the thickness of the aluminum film.[52]

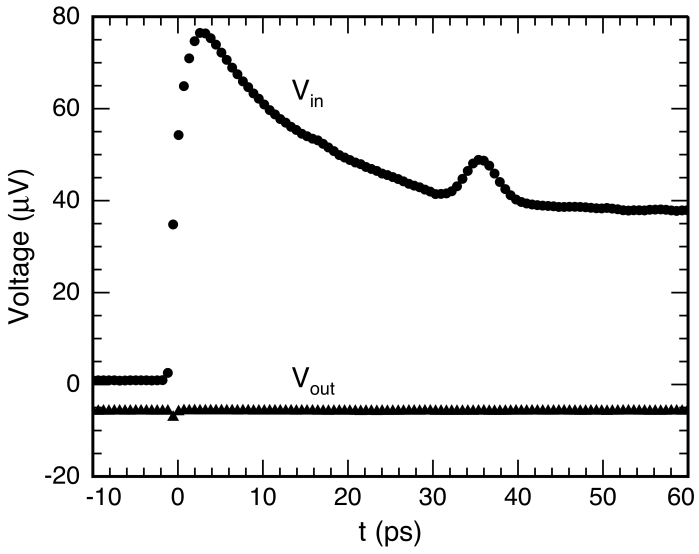

Figure 7: Sample TDTR data showing the in-phase (V_{in}) and out-of-phase (V_{out}) voltages as a function of delay time. Here t=0 corresponds to the time at which the pump and probe beams arrive simultaneously at the sample surface. These data show that the pump energy is absorbed in the aluminum film within 2-3 ps, after which the in-phase voltage decreases as the sample cools. The out-of-phase voltage remains nearly constant throughout the measurement. The fact that the out-of-phase voltage is constant is an easy way for us to check that the phase is set properly on the lock-in. Another interesting feature of the data at short delay times is the appearance of the acoustic echo at around t=35 ps. This acoustic echo is useful in accurately determining the thickness of the aluminum layer.

One significant source of error in the measurement is light from the pump beam reaching the photodetector. Since the photodetector and lock-in measure any incident light at the modulation frequency, it is critical that the reflected pump beam is completely blocked from reaching the photodetector. In order to keep the pump beam from reaching the detector, yet still allowing for the pump and probe beam to hit the same location on the sample, the pump and probe beams are adjusted to arrive at the sample through different angles of incidence. The probe beam passes straight into the back of the objective lens, and it is incident on the center of the sample. The probe beam is then reflected and goes directly back through the objective lens and into the photodetector.

The pump beam is adjusted so that it enters the back of the objective lens at a distance of 3-5 mm from the probe beam. With this separation distance, the pump is incident on the sample at an oblique angle of incidence, and it is then relatively easy to block the reflected pump beam and prevent light from the pump beam from reaching the photodetector. Along the same lines, a more troubling problem occurs with samples that are rough and scatter the pump beam. Light from the pump that is scattered along the probe beam path is impossible to eliminate using only beam blocks. The samples examined here were all smooth enough that the small amount of scattered light from the pump could be effectively eliminated using offsets on the lock-in since the amount of scattered light from the pump was small and constant through each measurement. For samples one must use additional techniques to eliminate the pump beam, such as using different wavelengths for the pump and probe beam, or going to a double modulation scheme where the pump and probe are modulated at different frequencies.[49, 53]

The photodetector measures the intensity of the reflected probe beam and the signal is passed through a resonant circuit (a simple RC circuit) to the RF lock-in amplifier in order to improve the signal-to-noise ratio. The purpose of the resonant circuit itself is to amplify the signal, and the RC circuit is tuned to the modulation frequency of the laser. The RF lock-in records the in-phase (V_{in}) and out-of-phase (V_{out}) components of the thermoreflectance signals, and we then use the ratio of the in-phase to out-of-phase voltages as a function of delay time up to ~3.5 ns for determining the thermal properties of our samples.

The $1/e^2$ beam diameters (where the intensity falls to $1/e^2 = 0.135$ times the maximum value) of the pump and probe beams are measured respectively by a Knife-

edge method [54] indicating the pump beam on the sample is 27 μm. The $1/e^2$ diameter for the probe beam is 23 μm when the delay stage is at the home position and 25 μm when the delay stage is at its longest delay time (about 600 mm away from the home position. The alignment of the pump and probe beams is aided greatly through the use of a CCD camera. Before collecting data, a beam splitter is placed in the optical path before the photodetector which allows us to visually inspect the sample surface. Here we can (a) move the sample stage so that the pump and probe beams are in focus at the sample surface, and (b) we can move the pump and probe beams so that they overlap at the surface. The CCD camera is also useful for locating features or regions of interest on the sample, or to avoid contamination or damaged regions.

In order to obtain quantitative results for thermal conductivity and interface thermal conductance, we compare the experimental results (i.e. the ratio $-V_{in}/V_{out}$) with a theoretical thermal transport model as shown in Figure 8 [47]. In general, for the types of samples measured in my work, we are able to extract both the thermal conductivity of the sample, and the interface conductance between the sample and the aluminum layer. These two properties are the fitting parameters, which are adjusted until the model and the data match.

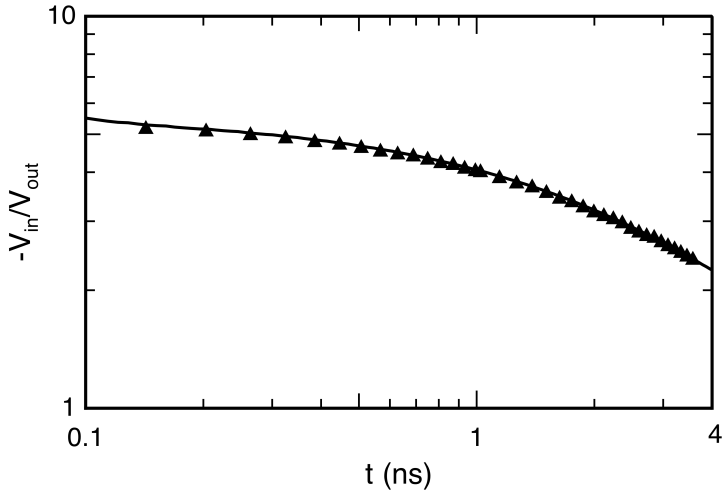

Figure 8: Sample experimental data (solid triangles) and best-fit from the thermal model (line). The in-phase (V_{in}) and out-of-phase (V_{out}) voltages are measured by the lock-in amplifier as a function of the delay time, t, between the pump and probe beams at the sample. The thermal conductivity of the sample and the interface thermal conductance between the aluminum film and the sample are used as fitting parameters in the thermal model, and these parameters are adjusted until the model fits the experimental data.

The thermal model is based on the solution to the heat diffusion equation for a periodic point source (i.e. the laser) on a semi-infinite solid, as given by Carslaw and Jaeger [55]. Since the laser energy is absorbed within the first 10-20 nm of the aluminum film, the heating may be considered to be a boundary condition. Since the pump and probe beam diameters are much greater than (a) the layers we are interested in examining, and (b) the penetration depth of the thermal wave in the sample, the heat flow is primarily one-dimensional, although we do account for three dimensional heat flow in the model. Starting with the general solution to the heat equation, the further refinements are made to allow for layered geometries [56], pulse accumulation, radial heat flow, and anisotropic thermal conductivities of the layers [57], as well as accounting for the change in the probe beam diameter due to beam divergence over the travel of the delay stage

[58]. The final development of the full model given in detail by Cahill [47], and the basic components of the model are described here.

The thermal response at the surface of the aluminum film depends on the thickness, thermal conductivity, and volumetric heat capacity of each material in the sample (including the aluminum film) as well as the thermal resistance at each interface between layers. Additionally, the laser repetition rate, the modulation frequency, and the pump and probe beam diameters must be included. Starting with the aluminum films, we take the heat capacity to be the same as for bulk aluminum, and we measure the thickness with the picosecond acoustics as mentioned previously. The thermal conductivity for the thin aluminum layers is reduced slightly from its bulk value, but it can be determined using the Wiedemann-Franz law [43] which relates the thermal conductivity of a metal to its electrical conductivity. Thus using a simple four-point-probe, or van der Pauw, measurement, we can accurately and rapidly determine the thermal conductivity of our thin aluminum layer. For all of the other layers in a sample, the heat capacity is also taken from bulk values in the literature, and thickness measurements for thin layers come from transmission electron microscopy (TEM) cross-sections. Samples where the thickness is greater than the penetration depth of the thermal wave can be treated as semi-infinite.

The interface between a pair of adjacent layers is represented in the model as a thin layer. Here the artificial layer is assigned a thickness of 1 nm so that there is no thermal capacitance in the layer (the heat capacity of the layer is irrelevant), and the thermal conductance, G, of the layer is then simply the ratio of the thermal conductivity of the layer to its thickness. Then, the remaining unknown parameters namely the thermal conductivity of an underlying layer and interface thermal conductance are adjusted until

the theoretical model matches the experimental data. It is important to point out that the interface conductance and the thermal conductivity affect the model in different ways. Changing the thermal conductivity essentially "offsets" the V_{in}/V_{out} data, while the interface conductance determines how quickly the ratio decays. In other words, it is not simply the total thermal resistance of the interface and sample that matters. The model is sensitive to whether the resistance is due to thermal conductivity or the interface resistance, thus we are able to extract both parameters simultaneously.

The entire data acquisition system, including the data recording from the lock-in, and the motion of the mechanical delay stage are computer controlled with a LabVIEW program created by Dr. Nitin Shukla. The LabVIEW control panel is shown in Figure 21 (in Appendix A). This image is taken from our current lab with new titanium:sapphire femtosecond laser (model #: Mai Tai HP) from Newport Inc.

3.2. Thermoelectric property measurement system

3.2.1. Design of the apparatus and hardware used in the system

In order to measure the thermoelectric properties of the new materials created in the lab of Prof. Shashank Priya and from our industry collaborator, Romny Scientific (San Francisco, CA), we required a new custom-made measurement system. While several commercial systems are available for measuring thermoelectric properties of bulk materials, these systems all have specific requirements for sample shape and size. It is not feasible to create large samples of a specific shape at this stage of our team's materials fabrication, thus we needed a unique system that could accommodate both thin film and bulk samples of various shapes, sizes, and thicknesses. Thus, I designed and built a thermoelectric property measurement system for measuring electrical resistivity and themopower (Seebeck Coefficient) of both thin films and bulk samples simultaneously over high temperature range of 20 to 350 °C [59]. In this section, the major components of the measurement system are described first, and the details of the electrical resistivity and thermopower measurements follow.

The apparatus is contained inside a 14 inch (diameter) x 18 inch (height) Pyrex bell jar with a cage supported by an aluminum stand, as shown in Figure 9. In addition to the apparatus inside the bell jar, this image also shows the equipment used for the measurements. Shown to the left of the bell are: (a) an Agilent 34970A switch which is used to switch the leads between thermal and electrical measurements, (b) a Keithley 6220 current source that supplies precise currents for the electrical resistivity measurements, and (c) a Keithley 2182A nano-voltmeter that allows for extremely

senstive voltage measurements. The experiments are entirely automated with a computer and LabVIEW program.

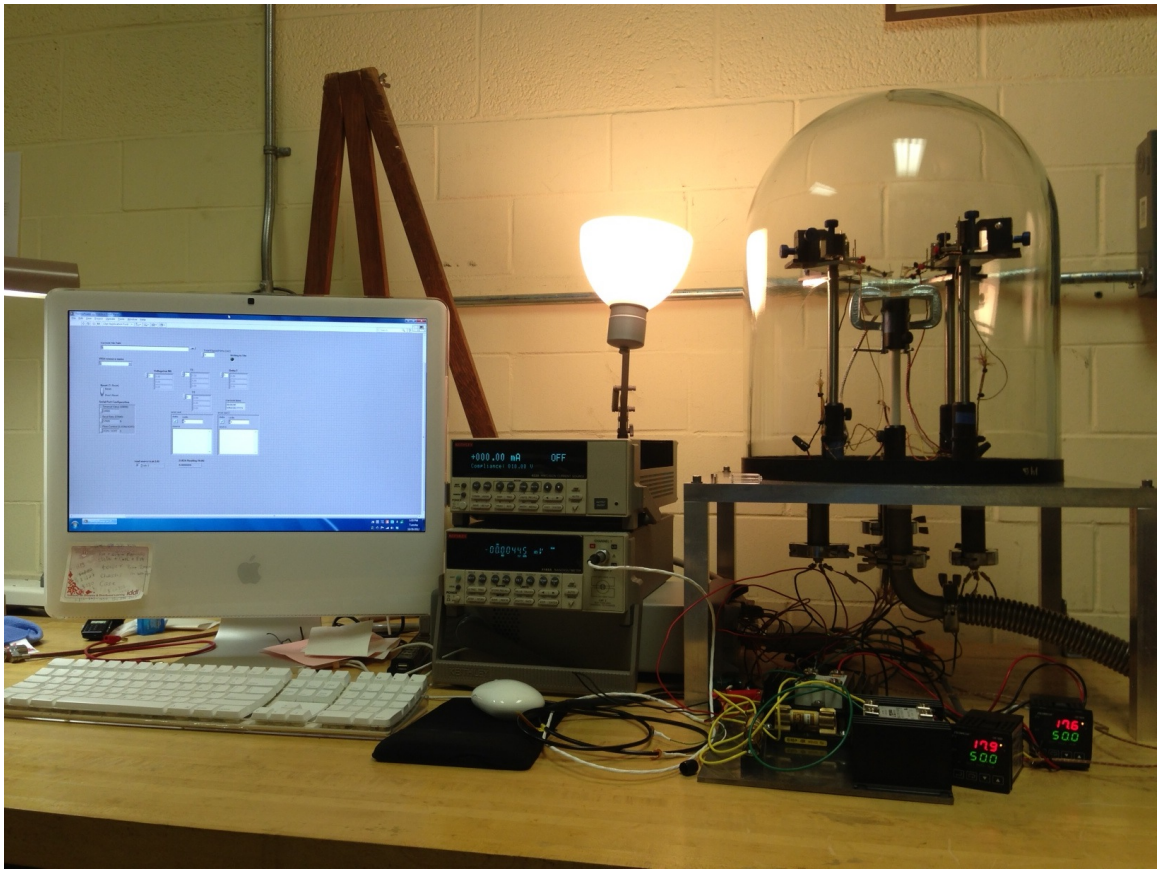

Figure 9: Thermoelectric property measurement system. The measurement appartus is contained within a Pyrex bell jar. There are five feedthroughs on the base plate of the bell jar that allow for a vacuum connection, electrical power to the heaters, as well as temperature and voltage measurements on the sample. Two Omega CN7832 temperature controllers combined with two solid-state realy and fuses are used to heat samples, and are shown in front of the bell jar stand. To the left of the bell are are an Agilent 34970A switch, a Keithley 6220 current source, and a Keithley 2182A nano-voltmeter. The measurements are automated with a computer and LabVIEW program.

Inside the bell jar the measurement system is located on a square 12 inch by 12 inch aluminum threaded base plate with five feedthroughs (four standard KF25 and one standard KF40 ports), as shown in Figure 10. The three standard KF25 ports are used for voltage measurements and to bring electrical power to the heaters, while the last KF25

port is connected to a turbomolecular vacuum pump. The one standard KF40 port used for a type K push-on thermocouple feedthrough. The measurements are performed in vacuum to eliminate errors associated with heat convection, and a stainless steel heat-shield is applied to reduce errors associated with thermal radiation losses.

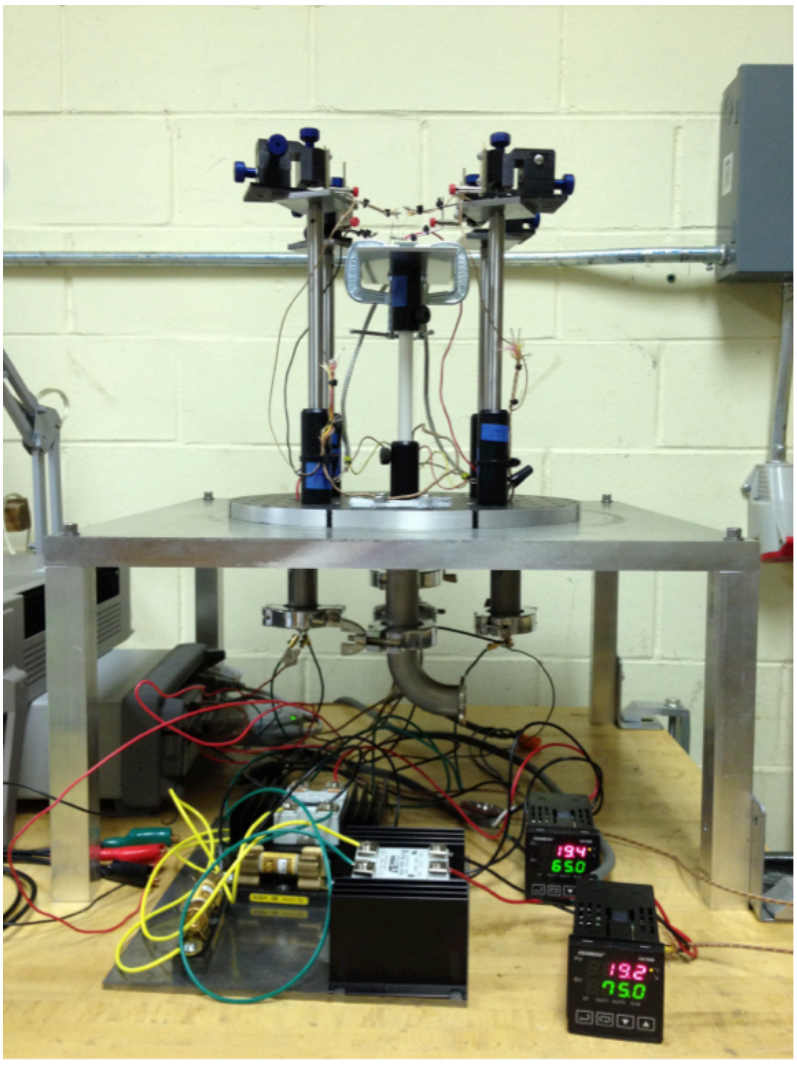

Figure 10: A closer look of the major components in the thermoelectric measurement apparatus. There are two manipulators in the front with thermocouple wires and two other manipulators in the back with tungsten probes. The manipulators are supported by four height-adjustable 8-inch tall posts screwed to the base plate. A zirconia ceramic rod (white rod in the center) is used to support an Inconel plate. The sample is placed on two boron-nitride blocks that contain two 200-Watt high-temperature cartridge heaters. Two clamps are used to adjust the distance between the two boron-nitride blocks so that we can measure samples of various sizes and shapes.

In order to perform measurements as a function of temperature, and to create the temperature gradient required for the Seebeck measurements, two cartridge heaters are used inside the bell jar. The cartridge heaters are inserted into two rectangular boron-nitride blocks, as shown in Figure 11. The heating power and temperatures of the heaters are controlled with two Omega CN7832 temperature controllers in conjunction with two solid-state relays and fuses as shown in front of the bell jar in Figure 10. The two cartridge heaters are fixed to the Inconel sample stage with two C-clamps, as shown in Figure 11. These C-clamps allow for easy movement and manipulation of the heaters so that the space in between the two boron-nitride blocks is adjustable and samples of various shapes and sizes can be measured in this system. Figure 12 depicts a schematic diagram of a cross-sectional view of the measurement system that corresponds to the photo in Figure 10. The Inconel sample stage is located at the center of the aluminum base plate, and it is supported with a zirconia ceramic rod.

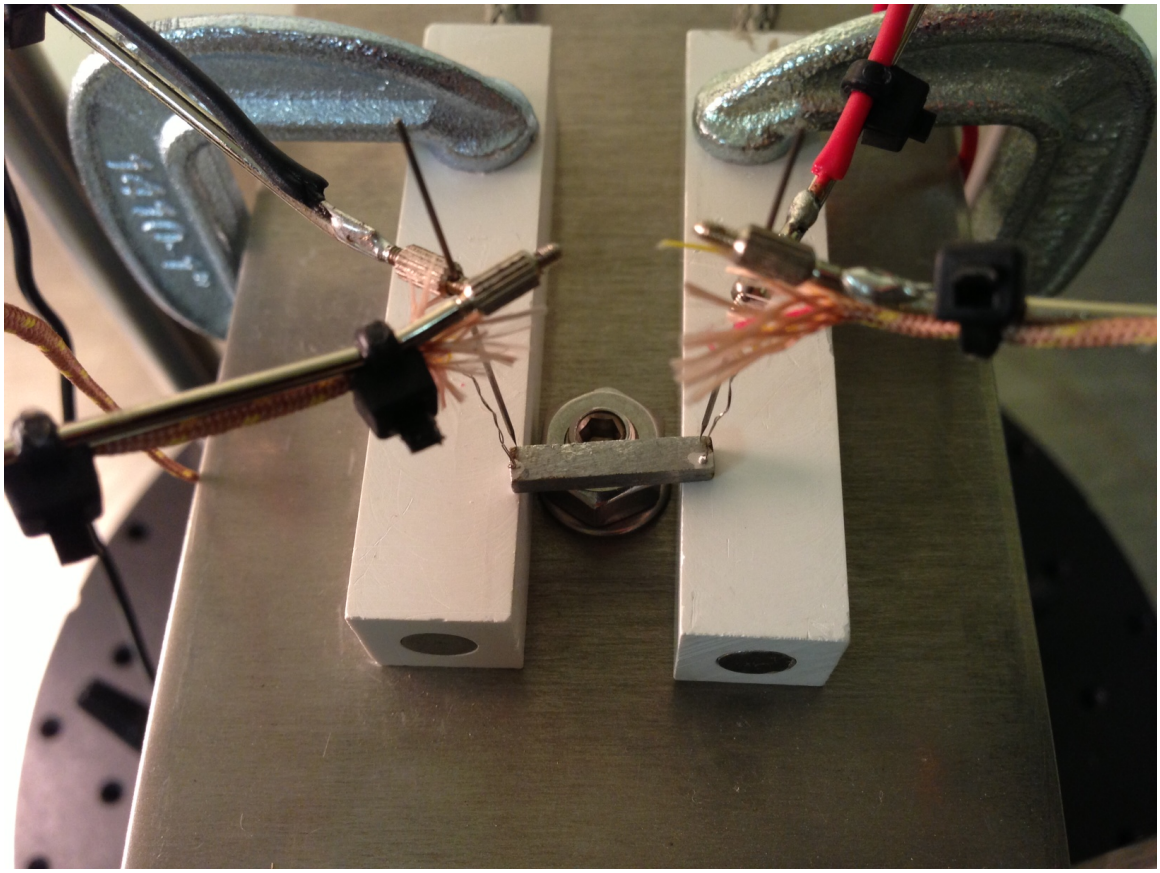

Figure 11: A top-view image taken from one of our testing sample, PbTe. The sample is the grey rectangular bar placed on the top of two boron-nitrite blocks. The two thermocouple wires that are thermally anchored to the sample using silver paint. They are attached to contact 3 & 4 while two tungsten probes are slightly attached to contact 1 & 2 corresponding to Figure 14.

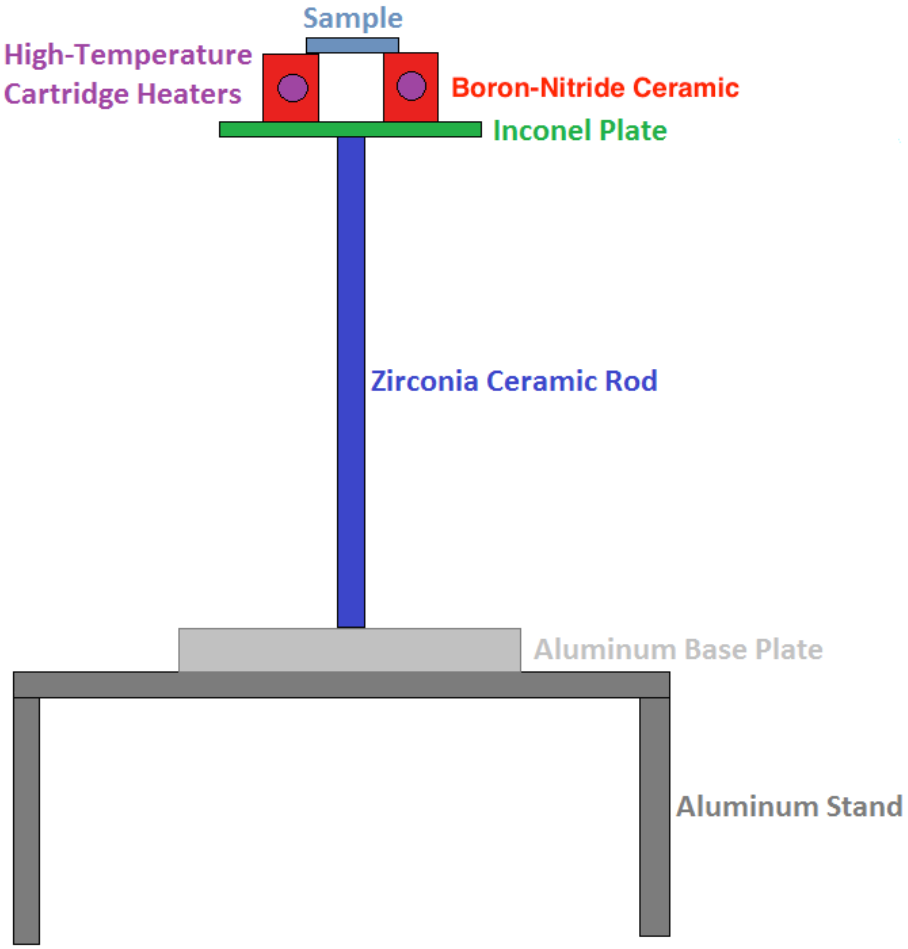

Figure 12: Schematic diagram of the thermoelectric measurement apparatus that corresponds with the photo in in Figure 10. The two cartridge heaters are inserted into two boron-nitride rods, and the samples are placed across the boron-nitride rods. The Inconel sample stage is separated from the aluminum base plate with a zirconia ceramic rod. Aluminum legs support the baseplate and allow for electrical and vacuum feedthroughs to be placed at the bottom of the baseplate.

The electrical and thermal measurements on the sample are aided with the use of four micro-manipulators as shown in Figure 10 and Figure 11. Two of the micromanipulators contain thermocouple wires that are thermally anchored to the sample using silver paint. The other two manipulators are fitted with tungsten probes for

electrical measurements. These four manipulators are supported by four height-adjustable 8-inch tall posts that are screwed to the aluminum base plate.

A block diagram of the measurement system is shown in Figure 13, and the basic operation of the unit can be described as follows. The bell jar is evacuated to the milliTorr range through the use a turbomolecular vacuum pump in order to eliminate measurement errors due to convection and/or radiation. The temperature at the sample and the temperature gradient across the sample are maintained with two cartridge heaters embedded in boron nitride rods, which are controlled with two Omega CN7832 temperature controllers. These temperature controllers are programmable, and the measurements can be done while temperature slowly ramps up or down without requiring attention from a user.

The Agilent 34970A switch unit, a Keithley 6220 current source, and a Keithly 2182A nano-voltmeter are connected with GPIB cables to a computer running a LabVIEW program I created for data acquisition and automation of the experiments. The Agilent switch unit allows us to use the thermocouple leads for measuring temperature and voltage, and we can rapidly switch between the measurements. The ability to switch the leads for voltage and temperature measurements external to the chamber, greatly improves our ability to make accurate Seebeck measurements and electrical resistivity measurements. For the Seebeck measurements, where we need to measure temperature and voltage and temperature at both ends of the sample, we use the thermocouple leads for both measurements as described in the following section. By using the same wires for the voltage and temperature measurements, this ensures that we are making our measurements at the same location, and we reduce errors that could be due to unknown

temperature gradients between voltage and temperature measurement locations that plague many Seebeck measurements. Further details of how the internal modules work in the Agilent 34970A are given in Appendix A (see Figure 23).

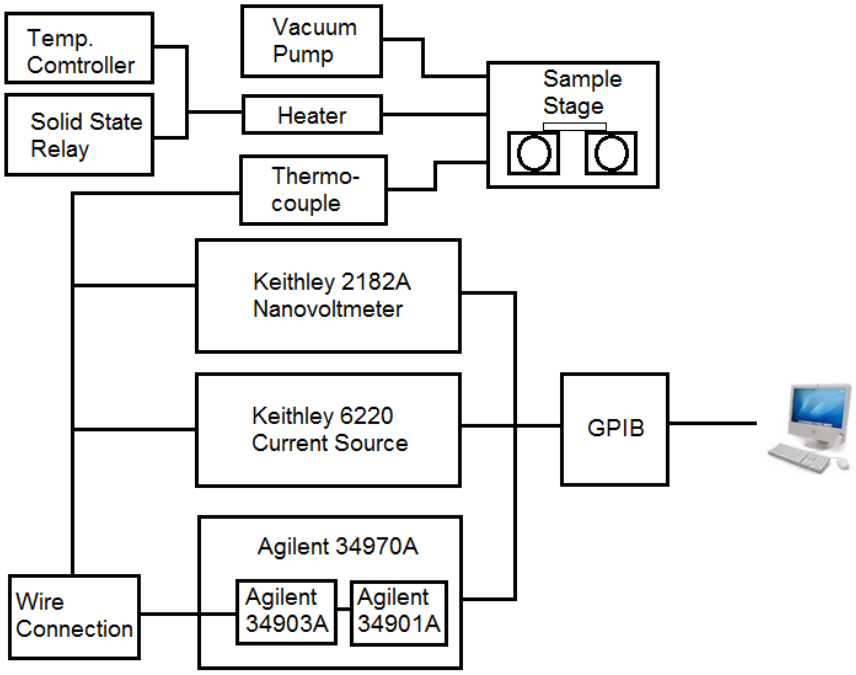

Figure 13: Block diagram of the thermoelectric property measurement system. The Agilent 34970A switch unit with two internal modules connects with a Keithley 2182A nano-voltmeter and a Keithley 6220 current source. These three devices are connected with a series GPIB cable to a computer running LabVIEW. The thermocouple wires and tungsten probes are wired to the two internal modules in the Agilent switch unit. The vacuum pump, temperature controllers, and thermocouples are connected to the chamber through standard KF ports.

3.2.2. Electrical resistivity measurements

The electrical resistivity of the thermoelectric samples is measured using the van der Pauw method [60]. The van der Pauw method can be used for flat arbitrary shaped samples as long as the sample meets certain requirements [61]. Specifically, the four

electrical contacts used in the measurement should be small, the contacts should be made at the perimeter of the sample, and the sample should be of uniform thickness where the thickness is much smaller than the diameter.

Figure 14 shows a schematic diagram of the van der Pauw measurement on a sample. Here, the four contacts are labeled 1, 2, 3 and 4 in a clockwise manner around the perimeter of a thin sample. Equation (3.1) defines the resistance $R_{12,43}$ and $R_{14,23}$

$$R_{12,43} = \frac{V_{43}}{I_{12}} \ , R_{14,23} = \frac{V_{23}}{I_{14}} \tag{3.1}$$

where V_{43} is the dc voltage measured between contacts 4 and 3 (or contacts 2 and 3 for V_{23}) and I_{12} is a supplied dc current that flows from contact 1 to contact 2 (or from contact 1 to contact 4 for I_{14}). The dc voltage across contacts 4 and 3 is measured using wires from the type K thermocouples on the sample. By using two of the wires already on the sample for the thermopower measurement we reduce the need for additional micromanipulators and probes in the measurement apparatus. Again we use the Agilent switch in order to appropriately select the proper lead for each measurement. In order to reduce the effect of unwanted thermoelectric voltages, the negative lead (alumel lead) are used in both contacts 4 & 3. After $R_{12,43}$ & $R_{14,23}$ are obtained, the electrical resistivity, ρ, can be determined by solving the van der Pauw equation:

$$\rho = \frac{\pi\, t}{\ln 2}\left(\frac{R_{12,43}+R_{14,23}}{2}\right)\cdot f \tag{3.2}$$

where t is the sample thickness, and f is a correction factor that depends on the ratio $R_{12,43}/\ R_{14,23}$ which is found in the literature [61].

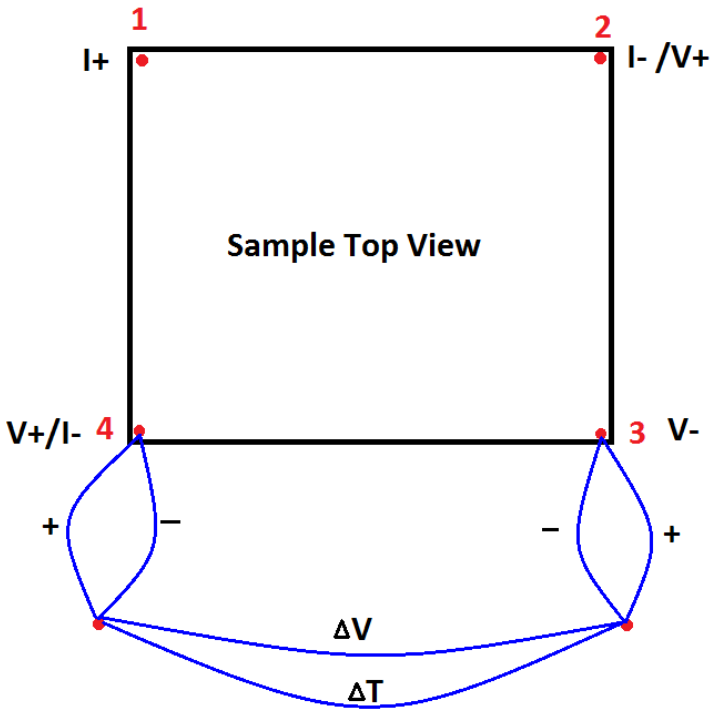

Figure 14: Schematic diagram of the top-view of a sample for the van der Pauw electrical resistivity measurements, and the thermopower (Seebeck coefficient) measurements. *I*+ and *I*- represent locations for the current supply, and *V*+ and *V*- give the locations for the voltage measurement. Here, ΔV and ΔT represent the measured dc voltage and temperature difference, respectively across contact 3 and 4. The voltage is measured by the negative lead (alumel lead) of type K thermocouple. The temperature and voltage measurements with the same lead(s) are done nearly simultaneously with the Agilent switch.

3.2.3. Thermopower (Seebeck coefficient) measurement

The Seebeck coefficient, or thermopower, of a material is defined as the voltage produced by the material when a temperature gradient is imposed on the material. Typical thermopower values are in the range of a few μV/K for metals to several hundred μV/K for semiconductors. Figure 15 shows a schematic diagram (side view) of a sample

measurement (a corresponding photograph from our actual experimental setup is shown in Figure 24). The absolute thermopower can be calculated using Equation (3.3) [10, 59].

$$S = -\frac{\Delta V}{\Delta T} + S_{ref.} \tag{3.3}$$

Here, S_{ref} is the Seebeck voltage generated within the alumel lead of type K thermocouple wire used for voltage measurement. This voltage is temperature dependent, so its absolute thermopower is taken into consideration in Equation (3.3).

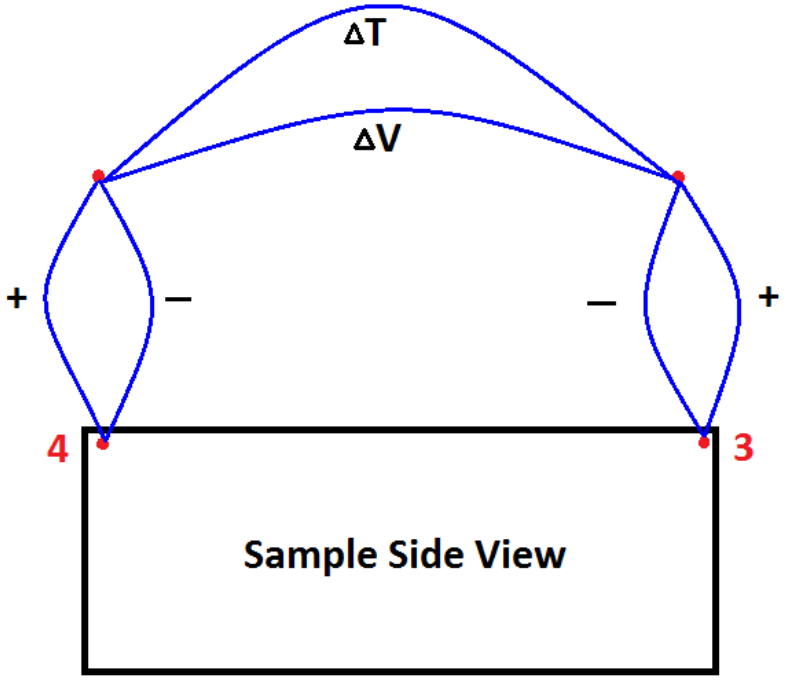

Figure 15: Schematic diagram of the sample for the Seebeck measurements. Similar to Figure 14, the ΔV and ΔT are the dc voltage and temperature across contact 4 and 3 and are taken nearly simultaneously (within one second) at the same locations using the Agilent 34970A switch unit. The dc voltage between contact 4 and 3 is measured with the alumel leads of the type K thermocouples at each location to avoid errors due to thermoelectric voltages generated in the leads.

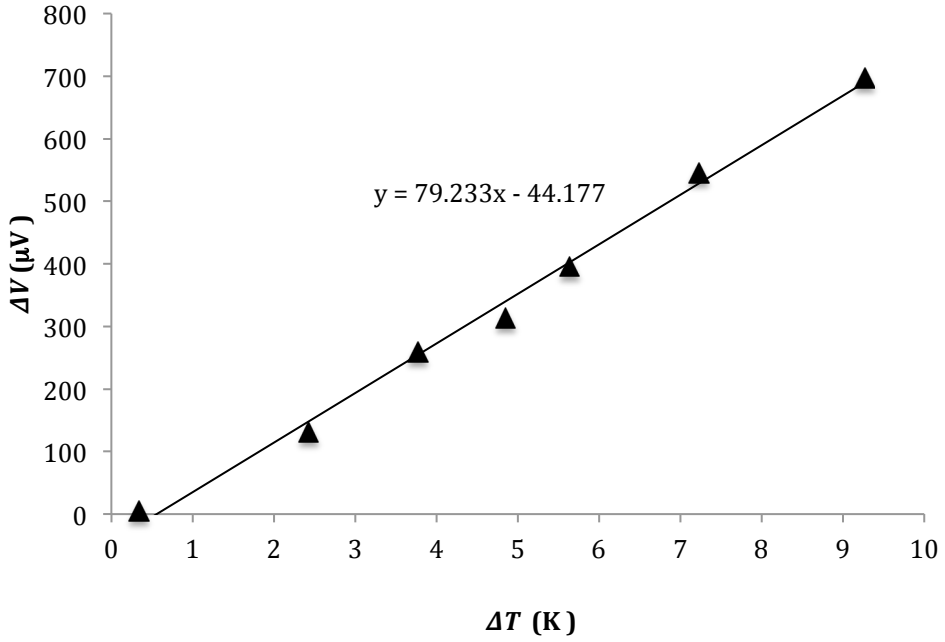

Figure 16: Thermoelectric voltage and temperature difference measured near room temperature on the PbTe-12%PbS disk grown by Zhao Yu in Prof. Priya's group. The thermopower is measured to be near 80 μV/K as indicated by the slope of the line on the plot.

A thermoelectric material, PbTe-12%PbS, is used for testing our thermopower system. This sample is from Prof. Priya's group in Materials & Science Department and was fabricated by one of our collaborators, Yu Zhao. The sample is ~ 10 mm in diameter and ~ 1 mm thick. Figure 16 is a measurement of the measured voltage difference plotted against the temperature difference near room temperature. The slope of the line gives the thermopower of PbTe-12%PbS to be ~80 μV/K.

3.3. Anter Flashline 3000 thermal diffusivity measurement system

The Anter Flashline 3000 thermal diffusivity measurement system (as shown in Figure 25 in the Appendix) is a commercial system made by Anter Corperation. This system is capable of measuring thermal diffusivity, α, as well as specific heat, C_p, for bulk materials at a temperature range from room temperature to ~500 ^{o}C. It provides a

nice compliment to our TDTR measurements of thermal conductivity. Once α and C_p are measured, the thermal conductivity, k, can be determined with the knowledge of density, ρ, from

$$\alpha = \frac{k}{\rho C_p}. \tag{3.4}$$

Table 3 shows a comparison of my thermal diffusivity measurements on a thermographite reference sample (# TGB1-B4-11-050) from Anter Corp, with results in the literature done by Maglic [62] in 2004. The sample size is 12.7 mm in diameter and 3.175 mm in thickness. We use this sample as a standard reference sample for our instrument, and the thermal diffusivity data shown in Table 3 are virtually identical to the accepted values.

Table 3: Thermal diffusivity of thermographite sample # TGB1-B4-11-050 measured from 50 to 220 ^{o}C by the Anter Flashline 3000 thermal diffusivity measurement system compared with literature values on the same reference material.

Temperature (^{o}C)	Measured Thermal Diffusivity (cm^2-S^{-1})	Thermal Diffusivity from Maglic[62] (cm^2-S^{-1})
57	0.51	0.51
119	0.44	0.43
170	0.38	0.38
222	0.33	0.34

4. Thermal conductivity of nano-crystalline Ni-18%Fe and Co-1.65%P alloys

Note: This chapter is based on a manuscript, "Thermal conductivity of nano-crystalline Ni-Fe and Co-P alloys," by Hao-Hsiang Liao, Ganesh Balasubramanian, Nitin C. Shukla, Chun-Hsien Wu, Li Li, Mitsuhiro Murayama, Peter K. Liaw, Ishwar K. Puri, and Scott T. Huxtable that will be submitted to *Applied Physics Letters* in December 2012, following final revisions/approval from all co-authors. I performed the experimental thermal conductivity and electrical conductivity measurements, analyzed the data, and wrote the manuscript. Ganesh Balasubramanian ran the molecular dynamics simulations under the supervision of Prof. Ishwar Puri. Chun-Hsien Wu and Prof. Mitsuhiro Murayama assisted with the electron microscopy measurements and interpretation of the measurements. Li Li and Prof. Peter Liaw (UT-Knoxville) gave insight on the nanoscrystalline alloys. Nitin Shukla and Prof. Huxtable provided advice in preparing and editing the manuscript.

Abstract

We examine the thermal conductivity of Ni-Fe (18% Fe by weight) and Co-P (1.65% P by weight) alloys using time-domain thermoreflectance (TDTR) measurements and compare our results with molecular dynamics (MD) simulations. The TDTR measurements give the total thermal conductivity of each alloy and the electron and phonon contributions to the thermal conductivity are extracted with electrical conductivity measurements and the Wiedemann-Franz law. The MD simulations confirm

the experimental measurements of the lattice conductivity, and the contribution of phonons to the overall thermal conductivity of these materials is much smaller than the electronic thermal conductivity. The fact that the simulations of the phonon thermal conductivity, which do not include grain boundaries, match the experimentally determined phonon thermal conductivity also indicate that the grain boundaries do not significantly scatter phonons in comparison with the alloy scattering.

While lattice vibrations, or phonons, are the major energy carriers in dielectrics and semiconductors, electrons dominate thermal transport in metals and conductors [63, 64]. In metallic alloys, the presence of two or more interacting lattices increases phonon-phonon, phonon-electron, and electron-electron collisions, which effectively reduces their thermal conductivity. However, thermal conductivity data of Ni alloys are limited since there are a wide range of possible alloys varying composition and traditional methods for determining thermal conductivity of these alloys are time-consuming and expensive to perform on numerous samples with a range of compositions [65]. There are data available for several Ni-Fe alloys, albeit with large variations and uncertainties between measurements done by different research groups [66]. While some of the variation in thermal conductivity data among research groups can be attributed to experimental error and uncertainty, a large amount of the variation is likely due to differences in the alloys beyond the fraction of Ni and Fe in the alloy. Specifically, different methods in producing the alloys can lead to large changes in the microstructure of the alloys, and electrodeposited Ni-Fe alloys can be created with grain sizes well below 100 nm [67, 68]. These nanocrystalline materials are known to possess larger electrical resistivity than alloys of the same composition but with large grain sizes due to the increased electron

scattering at the grain boundaries [69, 70]. Thus, we can expect that thermal conductivity will also vary significantly among nanocrystalline Ni-Fe alloys.

We investigate the electronic and phonon contributions to the thermal conductivity of nanocrystalline nickel-iron (18% Fe by weight) and cobalt-phosphorus (1.65% P by weight) alloys using a combination of fundamental molecular dynamics simulations and experimental measurements in order to understand and to predict the influence of varying composition on the thermal transport through these nanostructured materials. Nanocrystalline Ni-Fe and Co-P alloys are selected as the materials of interest because of their excellent material properties including improved hardness, yield strength, and ultimate tensile strength, along with relatively low thermal expansion coefficient and favorable magnetic properties. Their multifunctional properties make them useful for various applications where enhanced material performance, such as high strength, good tensile ductility, low thermal expansion, and corrosion resistance, are desirable. Thus, nanocrystalline alloys are attractive for many applications, such as thermostatic bimetals, glass sealants, electronic packages, and magnetic actuators [26-30].

Bulk nanocrystalline alloys containing Ni and 18% Fe, by weight, (Ni-18Fe) and Co and 1.65% P, by weight, (Co-1.65P) are fabricated by electrochemical deposition with a thickness of 3 mm in the deposition direction, were acquired from Integran Technologies, Inc. The as-deposited alloy has a single phase with a face-centered-cubic (fcc) structure [26, 27]. A transmission electron microscope (TEM) image of the Ni-18Fe alloy is shown in Figure 17. While under planar projection, the average grain size is shown to be roughly 25 nm. However, the grain size is nearly twice that size when

examined in cross-section [26]. The material exhibits a fiber texture [27] in the deposition direction composed of ellipsoidal shaped grains. Twins are also observed within some grains in the TEM micrograph, which is due to the low stacking fault energy in the alloy. The presence of the high density of grain boundaries in the alloy presents another barrier for phonon and electron transport. Both carriers experience significant scattering due to the alloying of two metals, but it is not clear what additional effect the nanocrystalline structure and high density of grain boundaries will have on either carrier.

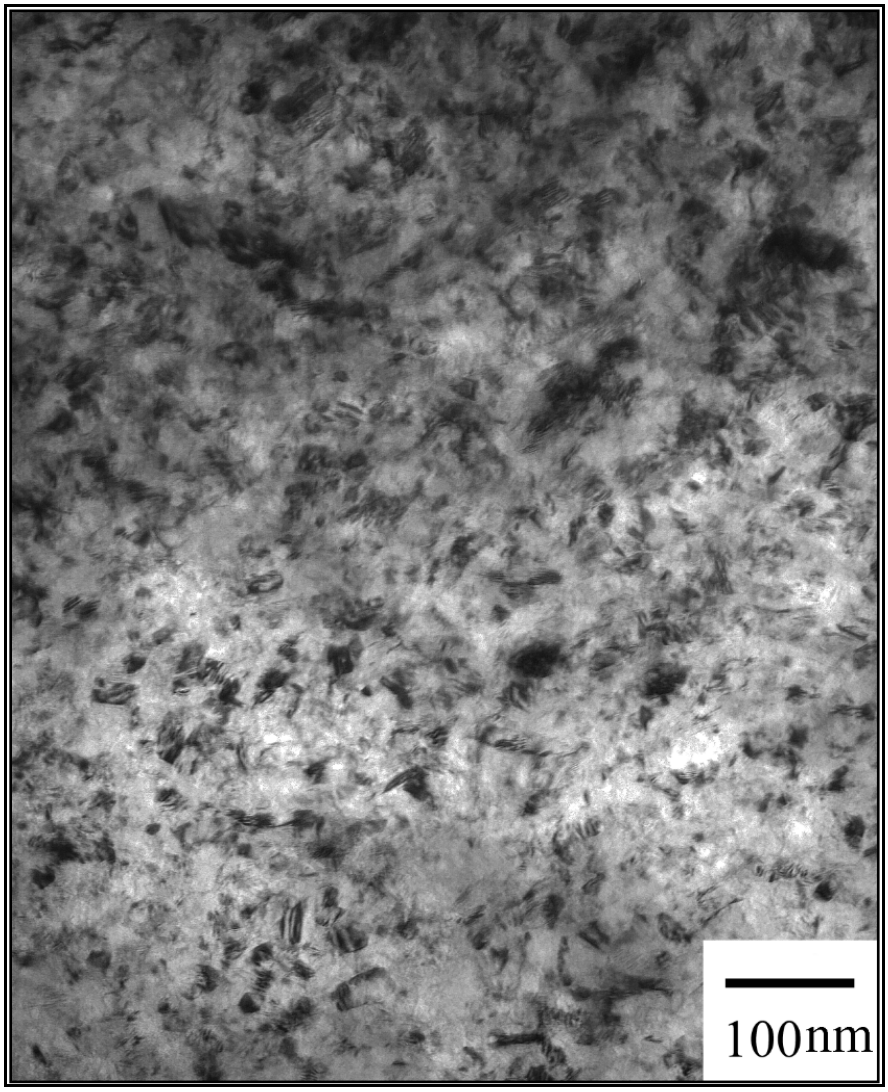

Figure 17: TEM micrograph of the Ni-18Fe specimen used in our experiments. This image was taken with the image plane perpendicular to the deposition direction.

The thermal conductivity, k, of each alloy is measured using time-domain thermoreflectance (TDTR) [2, 49]. TDTR is a pump-probe optical technique that measures thermal properties based on the thermally induced change in reflectivity of a thin aluminum film that coats each sample. A mode-locked ultrafast laser pulse (Coherent Mira Optima 900-F Ti:Sapphire) with a repetition rate of 76 MHz and wavelength of 780 nm is split into pump and probe beams. The pump beam is modulated at a frequency of f=9.86 MHz and is used to heat the aluminum film on the sample surface. The time-delayed probe beam reflects off of the aluminum layer and is directed into a photodetector. We measure this change in reflectivity for delay times up to 3.5 ns which gives a measure of the temperature decay at the surface of the sample. The $1/e^2$ beam diameter of the pump beam on the sample is 27 μm, and the probe beam diameter ranges from 23 μm to 25 μm over the 600 mm travel of the delay stage. A photodetector measures the intensity of the reflected probe beam and a lock-in amplifier records the in-phase (V_{in}) and out-of-phase (V_{out}) signals from the photodetector in order to improve the signal-to-noise ratio.

The thermal conductivity, k, of the material and the interface thermal conductance, G, between the aluminum layer and the material are extracted simultaneously by comparing the experimental data with a thermal model and adjusting k and G until the model matches the measurements [47]. The input parameters to the model include the thickness, heat capacity, and thermal conductivity for each layer in the sample. Interfaces are treated as thin layers (1 nm thick) where the interface conductance, G, is given by the ratio of the thermal conductivity to the thickness of the layer.

The 3 mm x 3 mm x 0.7 mm samples are each coated with a 93 nm Al layer using electron-beam evaporation. Aluminum exhibits a large change in reflectivity as a function of temperature at a wavelength of 780 nm. The Al layer thickness is verified through picosecond acoustic measurements performed with the same laser apparatus [52]. The volumetric heat capacities of the Ni-18Fe alloy, C_{NiFe} = 3.88 J cm^{-3} K^{-1}, and of the Co-1.65P alloy, $C_{Co\text{-}P}$ = 3.70 J cm^{-3} K^{-1}, are determined using the Kopp-Neumann Law. The heat capacity of the aluminum film is taken to be the same as for bulk aluminum, C_{Al} = 2.42 J cm^{-3} K^{-1}, and the thermal conductivity of the aluminum is determined to be k_{Al}= 180 W m^{-1} K^{-1}. The TDTR measurements give $k_{Ni\text{-}Fe}$ = 26 ± 4 W m^{-1} K^{-1}, $k_{Co\text{-}P}$ = 16.5 ± 2.5 W m^{-1} K^{-1}, $G_{Al/Ni\text{-}Fe}$ = 130 ± 20 MW m^{-2} K^{-1}, and $G_{Al/Co\text{-}P}$ = 80 ± 12 MW m^{-2} K^{-1}. The experimental data for the two alloys along with the "best-fit" curves from the TDTR model are shown in Figure 18.

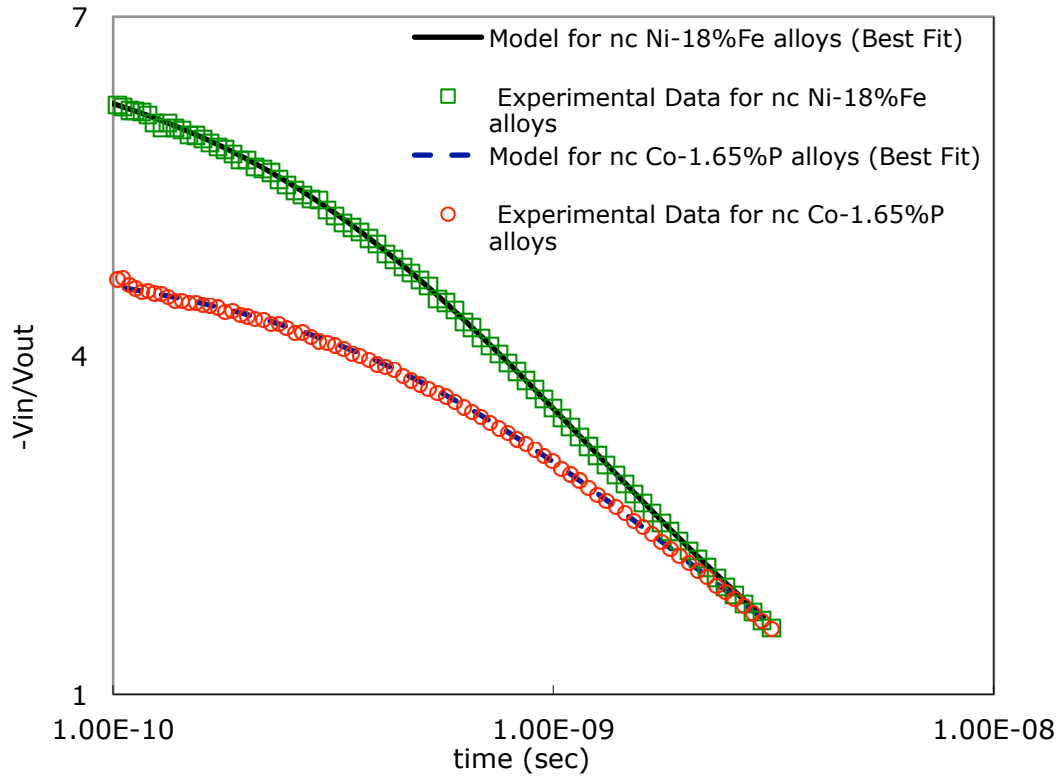

Figure 18: TDTR data for the Ni-18Fe and Co-1.65P samples. The vertical axis ($-V_{in}/V_{out}$) is the ratio of the in-phase to out-of-phase voltages from the photo detector as measured by the lock-in amplifier. The lines represent the best-fit curves from the thermal models. Where the interface conductance and the alloy thermal conductivity are the two fitting parameters.

The electrical resistivity of a metal can be related to the thermal conductivity of the material through the Wiedemann-Franz law, $k_e / \sigma = LT$, where σ denotes the electrical conductivity, T is the absolute temperature, and L is a constant called the Lorentz number, $L = 2.44 \times 10^{-8}$ W Ω K^{-2} [71]. Our room temperature measurements of the electrical conductivities for the Ni-18Fe and Co-1.65P alloys, give $\sigma_{Ni\text{-}Fe} = 3.36 \times 10^6$ S/m, and $\sigma_{Co\text{-}P} = 3.36 \times 10^6$ S/m. Therefore, the electronic contributions to the total thermal conductivity of each alloy are $k_{e,\,Ni\text{-}Fe} = 24.35$ W m^{-1} K^{-1} and $k_{e,\,Co\text{-}P} = 15.15$ W m^{-}

^{1} K^{-1}, leaving phonon contributions to thermal conductivity of $k_{p,\ Ni\text{-}Fe}$ = 1.65 W m^{-1} K^{-1} and $k_{p,\ Co\text{-}P}$ = 1.35 W m^{-1} K^{-1}. These experimental results are summarized in Table 4.

Table 4: Thermal properties of nanocrystalline Ni-18%Fe and Co-1.65%P at room temperature from our experimental results. The resistivity, ρ, is measured by the van der Pauw method, and the overall thermal conductivity is measured by TDTR. The electron thermal conductivity, $k_{e,}$ is calculated using the Wiedemann-Franz law in conjunction with our experimental measurement of electrical resistivity, ρ. The phonon thermal conductivity, k_p, is determined by subtracting k_e from the overall thermal conductivity, k.

Nanocrystalline alloys	Resistivity, ρ (Ω-nm)	Overall Thermal Conductivity, k (W/m-K)	Thermal Conductivity due to electron, k_e (W/m-K)	Thermal Conductivity due to phonon, k_p (W/m-K)	Interface Thermal Conductance, G (MW/m^{-2}-K)
Ni – 18 wt. % Fe	298	26.0 ± 4	24.35	1.65	130
Co – 1.65 wt. % P	480	16.5 ± 2.5	15.15	1.35	80

The phonon conductivities are comparable to the thermal conductivity of amorphous dielectric solids such as SiO_2, which is to be expected given the large amount of disordered in these materials due to the alloying and high density of grain boundaries [72, 73]. The relative contribution of the alloy scattering and grain boundary scattering are discussed in the following sections with additional insight given by the molecular dynamics simulations. The electronic contribution to thermal conductivity dominates and accounts for over 90% of the heat conduction in these alloys.

Before discussing the molecular dynamics simulations of these materials, we first turn our attention to the interface thermal conductance measurements. Our observed inductance values, $G_{Al/Ni\text{-}Fe}$ = 130 ± 20 MW m^{-2} K^{-1} and $G_{Al/Co\text{-}P}$ = 80 ± 12 MW m^{-2} K^{-1}, are smaller than typical conductance values of high quality metal-metal interfaces where

G is generally on the order of 0.5-1.5 GW $m^{-2} K^{-1}$ [74, 75]. Instead, we find G~100 $Wm^{-2} K^{-1}$, which is more typical of metal-semiconductor or metal-dielectric interfaces [49, 76]. Thus it seems likely that our metallic alloys contain a thin oxidation layer on the surface which reduces the thermal conductance.

We also employ detailed molecular dynamics (MD) simulations to further examine thermal transport in these nanostructured materials [77]. The simulations only consider the thermal transport through phonons, but the simulations give insight into the role of alloy scattering in comparison with grain boundary scattering. The phonon component of thermal conductivity, k_{ph}, is obtained from equilibrium MD simulations using the Green-Kubo method based on the fluctuation-dissipation theorem [77]. The heat current vector, S, in such systems oscillates about zero at equilibrium, and the thermal conductivity is correlated with the time required for these fluctuations to dissipate [2, 78-81]. Therefore, for a cubic isotropic material, $k_{ph} = (1/3k_B VT^2)\int_0^\infty \left\langle \vec{S}(t).\vec{S}(0) \right\rangle dt$, where k_B denotes the Boltzmann constant, V is the system volume, T is absolute temperature, t is time, and $\left\langle \vec{S}(t).\vec{S}(0) \right\rangle$ is the heat current autocorrelation function (HCAF). We determine k_{ph} from the converged values of the HCAF.

We eliminate system-size effects on the bulk thermal conductivity [2, 80-84] by specifying a 14 nm x 14 nm x 14 nm cubic Ni-18%Fe alloy block that contains 256,000 Ni and Fe atoms. Periodic boundary conditions eliminate phonon-boundary scattering and also ensure that the system is effectively infinite. Thus, the system is large enough to ensure that length-scale effects do not influence the simulated k_{ph} values. We point out that the model system does not account for any grain sizes or grain boundary scattering as well.

Multibody Embedded Atom Model (EAM) potentials [85, 86] are employed to describe the interactions between the Ni and Fe atomic sites. The system is initialized at a temperature of 300 K and simulated for 0.5 nanoseconds (ns) at constant temperature and pressure (NPT ensemble) using a Nose-Hoover thermostat and barostat. This arrangement ensures that the Ni-18Fe block is free of internal stresses and relaxes the system to its appropriate thermodynamic density. Next, the canonical (NVT) ensemble is imposed, and the system relaxes at constant temperature and volume for 0.5 ns after which an equilibrated system structure is obtained. Finally, equilibrium simulations are employed over the next 5 ns. The heat-current values are sampled over every 0.02 picoseconds (ps), and the time correlation between them is calculated. All simulations are employed using the LAMMPS code [87]. k_{ph} is calculated by averaging the thermal conductivities, k_{xx}, k_{yy} and k_{zz}, along the three orthogonal (x-y-z) directions of the cubic lattice. To accurately determine the HCAF integral, the simulation times should be much longer than the phonon relaxation time of ~100 ps (> 5 ns) [81, 83].

The variations in k_{xx}, k_{yy}, and k_{zz} are shown in Figure 19. These values are obtained by integrating the HCAF over time. The thermal conductivity initially increases for ~1 ns due to oscillations in the HCAF, followed by a gradual decay to a constant value after ~2.5 ns. The initial increase in k_{ph} is attributed to equilibrium fluctuations, which gradually dissipate after being averaged over longer times. The time required for the fluctuations to recede, when a converged value of the HCAF can be determined, is directly proportional to the largest phonon relaxation time in the material [83]. Systems in which k_{ph} has a large contribution to k should therefore typically require simulations of O (~10^1-10^2 ns). This qualitative analysis leads us to predict that the contribution of

phonons to k for Ni-18Fe is limited. The average value of the HCAF integral between 3.5 - 4.5 ns (which is the shaded region in the inset of Figure 19) is used find $k_p = 1.74$ W m^{-1} K^{-1}, which is comparable to the experimentally determined value of $k_p = 1.65$ W m^{-1} K^{-1}, and is also much smaller than k_e. The fact that the simulations, without accounting for any grain boundary scattering, predict k_p that is nearly identical to the experimentally measured value indicates that the influence of the grain boundaries on phonon scattering is minimal and that alloy scattering is the dominant form of thermal resistance for the phonon thermal conductivity.

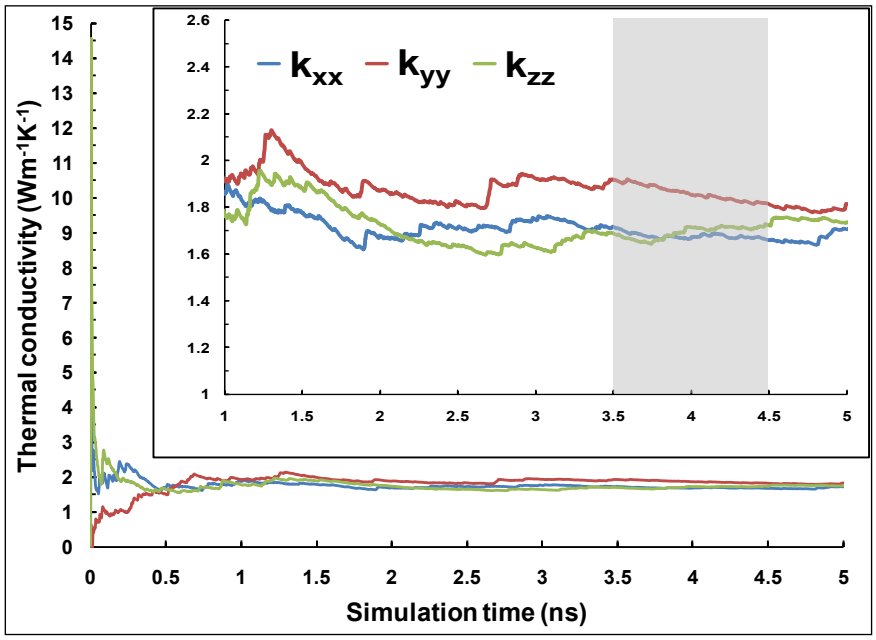

Figure 19: The phonon thermal conductivity over time evaluated by integrating the heat current autocorrelation function (HCAF). The thermal conductivity first increases along all three orthogonal directions (x-y-z), then decreases and becomes constant at longer times when the autocorrelation function decays to zero. The inset shows the time evolution of k_{xx}, k_{yy} and k_{zz} after 1 ns of simulation time when the variations in their values occur about an average value. The average Ni-18Fe k is sampled along the three orthogonal directions in the shaded region.

Making the material more internally heterogeneous, or incorporating other conductive impurities or materials in the alloy, should further lower k due to internal

scattering between phonons and electrons [88]. We also simulate cases with 40% and 60% Fe by weight in the alloy to investigate the influence of composition on the thermal conductivity, k_{ph}, values which are presented in Table 5. The thermal conductivity does not change significantly although k_{ph} is slightly larger for the Ni-40Fe alloy. This indicates that the alloy scattering is essentially saturated with 18% Fe and increasing the amount of iron in the alloy does not appreciably scatter any additional phonon modes.

Table 5: Thermal conductivity of Ni-Fe alloys obtained from MD simulations with 18, 40 and 60 weight percent of Fe, respectively.

Case	Weight % of Iron (Fe)	Thermal Conductivity due to phonon, k_p (W/m-K)
1	18	1.74
2	40	1.89
3	60	1.70

In summary, we have examined the thermal conductivity of Ni-18%Fe and Co-P alloys through TDTR measurements and equilibrium MD simulations. This work demonstrates that the prime contribution to the bulk thermal conductivity is due to the movement of free electrons in the alloy rather than phonon transport, which is more than an order of magnitude smaller. Furthermore, we found that the small phonon thermal

conductivity was due to alloy scattering rather than grain boundary scattering. Varying the fraction of Fe in the alloy can increase k_{ph} by a small but not significant amount.

The authors thank Krishna Vummidi of Virginia Tech for his advice. G.B. thanks the Virginia Tech Department of Engineering Science and Mechanics for use of its LCC supercomputing cluster. P. K. Liaw greatly appreciates the support of the National Science Foundation (DMR-0909037, CMMI-0900271 and CMMI-1100080 with Dr. A. Ardell and Dr. C.V. Cooper as program directors). S. T. Huxtable gratefully acknowledges support from the National Science Foundation (CBET-0547122).

5. Thermal properties of bulk metallic glasses (BMGs)

5.1. Introduction

In 1960, Klement and his colleagues [89] from Caltech developed the first bulk metallic glass, gold–silicon alloys, by creating an innovative quenching technique for chilling metallic liquids at very high rates. Fifty years later, bulk metallic glasses (BMGs) have since become well-known for their great strength, hardness, toughness, and corrosion resistance which are promising for various applications such as sporting goods, bicycle frames, corrosion resistant materials, machinery tools, etc. [31] In contrast to the widely studied mechanical behavior of bulk metallic glasses [90], thermal properties of BMGs remain largely unexplored and the vibrational features in BMGs are poorly understood. In micro/nanoscale heat transfer, the length scale of devices is comparable to the mean free paths and/or wavelengths heat of carriers such as phonons and electrons. Therefore, a better understanding of vibrational modes and how they impact phonon thermal conductivity in these metallic alloys become essential.

Unlike crystalline structures, bulk metallic glasses have a unique amorphous structure that can provide the fundamental understanding of how thermal properties are affected by the behavior of the phonon and electron in the environment lacking of ordered atomic arrangement. Recent studies[91-93] indicate that localized harmonic vibrations may exist in BMGs. As a consequence, the specific heat is mediated by phonons in BMGs, and the specific heat may be described by the Debye model The Debye model includes a featureless density of states (DOS), plus an additional Einstein mode, which describes the localized harmonic vibrational mode with a specific frequency. It is important to understand the importance of the Einstein mode on the

thermal properties in amorphous materials, such as BMGs [93].

In this work, we are examining four different compositions of BMGs, $Zr_{50}Cu_{40}Al_{10}$ (Zr-BMG), $Cu_{46.25}Zr_{44.25}Al_{7.5}Er_2$ (Cu-BMG), $Fe_{48}Cr_{15}Mo_{14}C_{15}B_6Er_2$ (Fe-BMG), and $Ti_{41.5}Zr_{2.5}Hf_5Cu_{42.5}Ni_{7.5}Si_1$ (Ti-BMG). All subscripts give the atomic percentage of each component. These samples are grown in Prof. Peter K. Liaw's group in the Department of Materials Science & Engineering at the University of Tennessee at Knoxville [90, 94, 95].

5.2. Experimental procedure

First, each metallic glass is coated with a reflective aluminum layer (~90 nm in thickness) using electron beam evaporation in the cleanroom in the Electrical and Computer Engineering Department at Virginia Tech. The aluminum thickness is calculated by measuring the round trip time for acoustic echoes to travel through the aluminum film [96] and using the speed of sound, 6420 m/s, in aluminum [97].

The thermal conductivity, k, of the four BMGs and the interface thermal conductance, G, between the aluminum film and each BMG are measured using the time-domain thermoreflectance [47-49] technique that is described in detail in Chapter 3. The thermal conductivity and interface thermal conductance are extracted by comparing the experimental data to the theoretical thermal transport model created by Cahill [47]. The input parameters to extract the thermal conductivity and the interface thermal conductance are the laser modulation frequency (~9.86 MHz), pump and probe beam diameters, heat capacity, aluminum layer thickness, and the thermal conductivity for each layer. The heat capacities for the BMGs are calculated using the Kopp-Neumann law [98].

We model each interface as a 1 nm thick layer, and the interface thermal conductance is found from the ratio of the thermal conductivity to the thickness of the layer.

The electronic contribution to the thermal conductivity, k_e, is determined using the the Wiedemann-Franz law, $k_e / \sigma = LT$, where σ is the experimentally measured electrical conductivity (inverse of electrical resistivity), T is the temperature, and L is the Lorentz number, $L = 2.44 \times 10^{-8}$ W Ω K^{-2} [71], The phonon, or lattice, contribution to the thermal conductivity, k_p is determined by subtracting k_e from the overall thermal conductivity, k.

5.3. Results and discussion

Figure 20 displays the experimental data taken by TDTR and the best fit curves from the theoretical thermal transport model on the four BMG samples. Here we see excellent fits between our data and our model. The measured thermal conductivity and interface conductance values are shown in Table 6. There are several interesting features in these results. First, as we would expect for amorphous disordered systems, the phonon contribution to thermal conductivity is small for all four samples. The electrical conductivity is low for the metallic alloys, but again, one would expect to observe a significant reduction in electrical conductivity as well due to the increased alloy scattering.

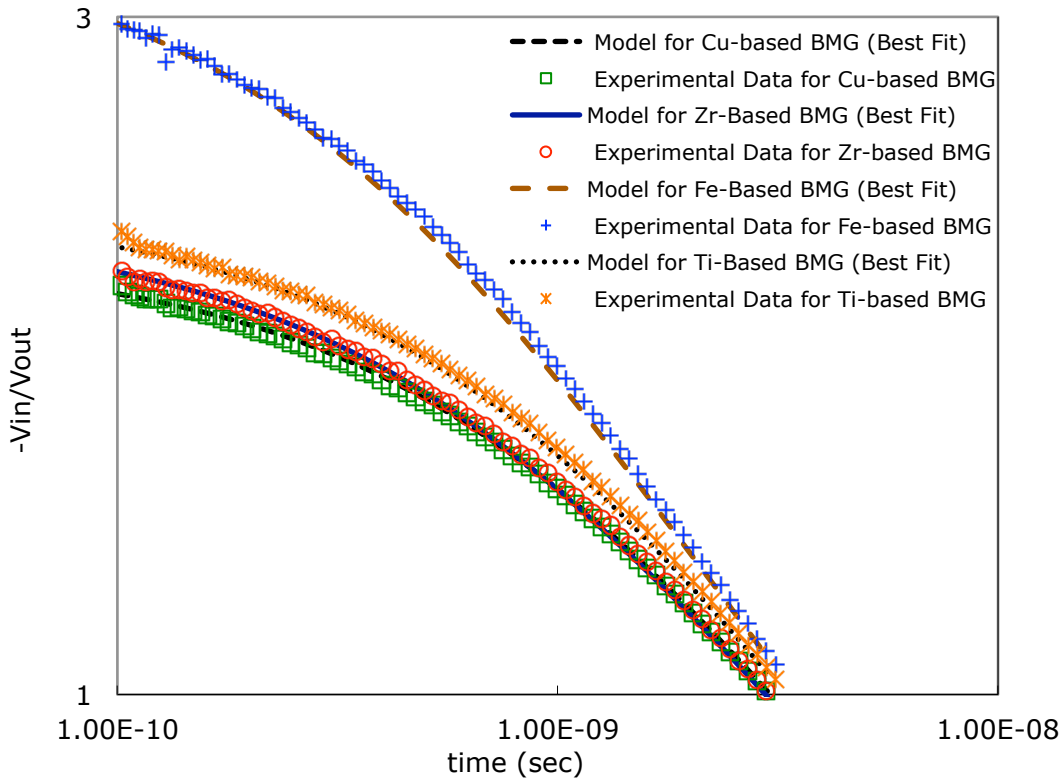

Figure 20: Time-domain thermoreflectance data and the best fit curves of the theoretical thermal transport model on the Cu-based BMG (□), Zr-based BMG (O), Fe-based BMG (+), and Ti-Based BMG (*). On the vertical axis "V_{in}/V_{out}" represents the ratio of the in-phase to out-of-phase voltage at the photodetector as measured by a lock-in amplifier. The time on the horizontal axis refers to the delay time between the arrival of the pump and probe beams.

Table 6: The thermal properties of four different types of bulk metallic glasses at room temperature from our experimental results. The resistivity, ρ, is measured by van der Pauw method, and the overall thermal conductivity is measured by TDTR. The electron thermal conductivity, $k_{e,,}$ is calculated by Wiedemann-Franz law from the experimental result of resistivity, ρ. The phonon thermal conductivity, k_p, is determined by subtracting k_e from the overall thermal conductivity, k.

Amorphous BMGs	Resistivity, ρ (Ω-m)	Overall Thermal Conductivity, k (W/m-K)	Thermal Conductivity due to electrons, k_e (W/m-K)	Thermal Conductivity due to phonon, k_p (W/m-K)	Interface Thermal Conductance, G (MW/m^{-2}-K)
$Zr_{50}Cu_{40}Al_{10}$ Amorphous BMG	2.57×10^{-6}	4.1 ± 0.6	2.83	1.27	120
$Cu_{46.25}Zr_{44.25}Al_{7.5}Er_2$ Amorphous BMG	2.11×10^{-6}	3.9 ± 0.6	3.45	0.45	90
$Fe_{48}Cr_{15}Mo_{14}C_{15}B_6Er_2$ Amorphous BMG	1.32×10^{-6}	6.2 ± 0.9	5.51	0.69	180
$Ti_{41.5}Zr_{2.5}Hf_5Cu_{42.5}Ni_{7.5}Si_1$ Amorphous BMG	2.19×10^{-6}	4.0 ± 0.6	3.32	0.68	84

We see that the Fe-BMG has the highest overall thermal conductivity (k = ~ 6.2 W/m-K), and the lowest electrical resistivity (ρ = ~1.32×10^{-6} Ω-m). However, there are two interesting features of this sample. One, the phonon thermal conductivity is quite low

at k_p = 0.7 W m^{-1} K^{-1}. Thus, while this alloy significant scatters phonons, the electron transport is not hindered as significantly as the other BMGs. Another significant feature of this material is the large interface thermal conductance of. $G_{Fe\text{-}BMG}$ = 180 MW m^{-2} K^{-1}. Given the comparatively large electrical conductivity for this sample, it seems likely that this large interface conductance is due to efficient electron-electron coupling at the interface.

The Zr-BMG and Cu-BMG also have a few interesting features. First, these two samples are similar in composition with regards to Zr (50% vs. 44.25%), Cu (40% vs. 46.25%), and Al (10% vs. 7.5%), but the Cu-BMG contains 2% Erbium while the Zr-BMG does not contain any Er. Despite the large degree of similarity in composition, the Zr-BMG has a phonon thermal conductivity nearly a factor of three larger than the Cu-BMG. While the primary difference between the two samples is the small amount of Erbium in the Cu-BMG, this is a significant change in terms of phonon transport. The other elements in these two samples are relatively light – Al (26.98 atomic weight), Cu (63.55), Zr (91.22) – Er has an atomic weight of 167.26. When considering the lattice as a spring-mass system, this small amount of a significantly heavier element can dramatically disrupt phonons. Zheng *et al*. [99] examined a series of $(InGaAs)_{0.8}(InAlAs)_{0.2}$ segmented elements containing 0.0, 0.3 and 3% Er, and found room temperature values of ~ 4 W m^{-1} K^{-1}, 3 W m^{-1} K^{-1}, and 2 W m^{-1} K^{-1} for the three samples, respectively, indicating that even small amount of Erbium can cause a substantial amount of additional phonon scattering. Kim *et al*. [100] found that with the addition of ErAs nanoparticles, they could reduce thermal conductivity of $In_{0.53}Ga_{0.47}As$ to almost a factor of two below the so-called "alloy limit." Our work confirms these

findings, and demonstrates that further reductions in thermal conductivity are possible even for highly disordered alloys that already contain significant phonon scattering. The other interesting aspect of the Erbium content is that it does not seem to produce as significant of an amount of scattering with the electrons. Thus the inclusion of a small amount of high mass atoms may be a route for reducing thermal conductivity without as strong of a reduction in electrical transport for thermoelectric materials.

While the Cu-BMG and Fe-BMG have low phonon thermal conductivities – presumably due in large part to the 2% Erbium – the Ti-BMG also exhibits small phonon thermal conductivity. While the Ti-BMG does not include any Er, it does have 5% Hafnium which has an atomic weight of 178.49. Thus it seems likely that that Hf acts in a similar manner to reduce the phonon thermal conductivity in this sample.

Additionally, it is worth noting that the thermal conductivity of the $Zr_{50}Cu_{40}Al_{10}$ BMG, k = 4.1 W/m-K is in good agreement with measurements done by Yamasaki *et al*. for similar BMGs of $Zr_{41}Ti_{14}Cu_{12}Ni_{10}Be_{23}$ [101], k=4.6 W/m-K, and $Zr_{55}Al_{10}Ni_5Cu_{30}$ [102], k = 5.0 W/m-K. Also, in work from our group that I co-authored with Shukla *et al*. [98], we found k=4.5 W/m-K for a BMG of $Zr_{47}Cu_{31}Al_{13}Ni_9$. These similar results on comparable BMGs provide further evidence that the primary mechanism for further reduction in thermal conductivity in the Cu-BMG is the inclusion of the small amount of high mass atoms.

6. Additional Contributions Published Elsewhere

In addition to the work described in this dissertation, I have also made contributions to other work done in Prof. Huxtable's lab during my time at Virginia Tech. While some of this work is still ongoing, two other projects led to publications in *Applied Physics Letters* by Shukla et al. [98, 103] in which I was the second author, and a third manuscript in which I was also the second author, by Shukla et al. [104] that was presented at a conference and will be submitted to a journal soon. In all three studies my contributions were with the experimental setup and data collection.

In the first paper [98], we used TDTR to examine crystalline and amorphous metallic alloys of $Zr_{0.47}Cu_{0.31}Al_{0.13}Ni_{0.9}$ with a Y_2O_3 coating. We found that the crystalline alloy had a slightly larger thermal conductivity, (5.0 W m^{-1} K^{-1} for the crystalline alloy compared to 4.5 W m^{-1} K^{-1} for the amorphous alloy) owing to a larger phonon thermal conductivity in the crystalline lattice. Interface thermal conductance measurements gave smaller conductance between the Y_2O_3 and the alloys than for the aluminum/Y_2O_3 interfaces, due to the smaller electrical conductivity of the metallic alloys as compared with the aluminum film.

The second article [103] deals with thermal transport in nanostructured composites of yttria stabilized zirconia embedded with nickel nanoparticles of varying diameter. In this work we were able to extract the interface thermal conductance of the embedded nanoparticles and found G > 170 MW m^{-2} K^{-1}. This was one of the first studies where the interface thermal conductance of buried nanoparticles was measured experimentally.

Finally, we examined a series of GaN thin films that were grown by metal-organic chemical vapor deposition (MOCVD) by Prof. Lou Guido in the Materials Science Department at Virginia Tech [104]. Here we examined the role that dopants, defects, and dislocations have on thermal transport in thin GaN films. We found that dislocations due to film thickness were the controlling mechanism for determining thermal conductivity variations between samples.

7. Summary

The significant contributions of this work include both the development and refinement of advanced thermal and thermoelectric measurement systems, as well as improved understanding of thermal behavior in several nanostructured material systems. Overall, my work has improved our ability to rapidly obtain thermal properties for a variety of nanostructured materials – both in thin film form and nanostructured bulk composites. Additionally, the materials we examined have not only provided useful property data, but also insights into the fundamental mechanisms that control heat transport in complex nanostructured systems. These insights should be useful to others working in the community where controlling heat conduction at the nanoscale is a route towards improved materials and more efficient devices.

Time-domain thermoreflectance systems have recently emerged as useful tools for nanoscale thermal characterization. These systems are still evolving and today there are perhaps 15-20 laboratories in the world with some form of a TDTR system, while 10 years ago there were less than five. My contributions here were developing schemes for controlling the pump and probe beam diameters, while reducing measurement errors, improving sensitivity, and still allowing for ease of use for other students doing measurements on liquids and nanoparticle suspension. Furthermore, we designed, refined, and assembled our system to work with three different lasers is a total of four separate laboratories during my PhD studies.

In the area of thermoelectric property characterization, I designed and assembled a thermoelectric property measurement system capable of measuring electrical conductivity and Seebeck coefficient from room temperature up to 350 °C on samples

with various shapes and sizes in order to handle the many different types of samples produced with several fabrication techniques by our collaborators on campus and in industry. As more samples become available, this system will be useful in the rapid and accurate determination of the thermoelectric properties of a variety of new materials fabricated by collaborators. These thermoelectric property measurements will be critical in order to determine the structure-property relationships required to evaluate and improve the newly developed TE materials.

Using these tools, we examined several nanostructured material systems. I studied two different types of nanocrystalline metallic alloys composed of nickel-iron and cobalt-phosphorus. My results indicated that the thermal conductivity of the nanocrystalline alloys was reduced by a factor of roughly two from the thermal conductivity measured on metallic alloys with larger grain sizes. Corresponding molecular dynamics simulations done by a colleague, and my own electrical conductivity measurements, demonstrated that this strong reduction in thermal conductivity was the result of increased electron scattering at the grain boundaries, and that the phonon component of the thermal conductivity was largely unchanged by the grain boundaries.

I also examined four complex bulk metallic glass (BMG) materials. From these measurements, we found that the addition of even a small percentage of heavy atoms (i.e. Hf and Er) into the complex disordered BMG structures created a significant reduction in the phonon thermal conductivity of these materials. The work also showed that the addition of these heavy atoms does not disrupt electron transport as strongly as phonon transport.

Appendix A

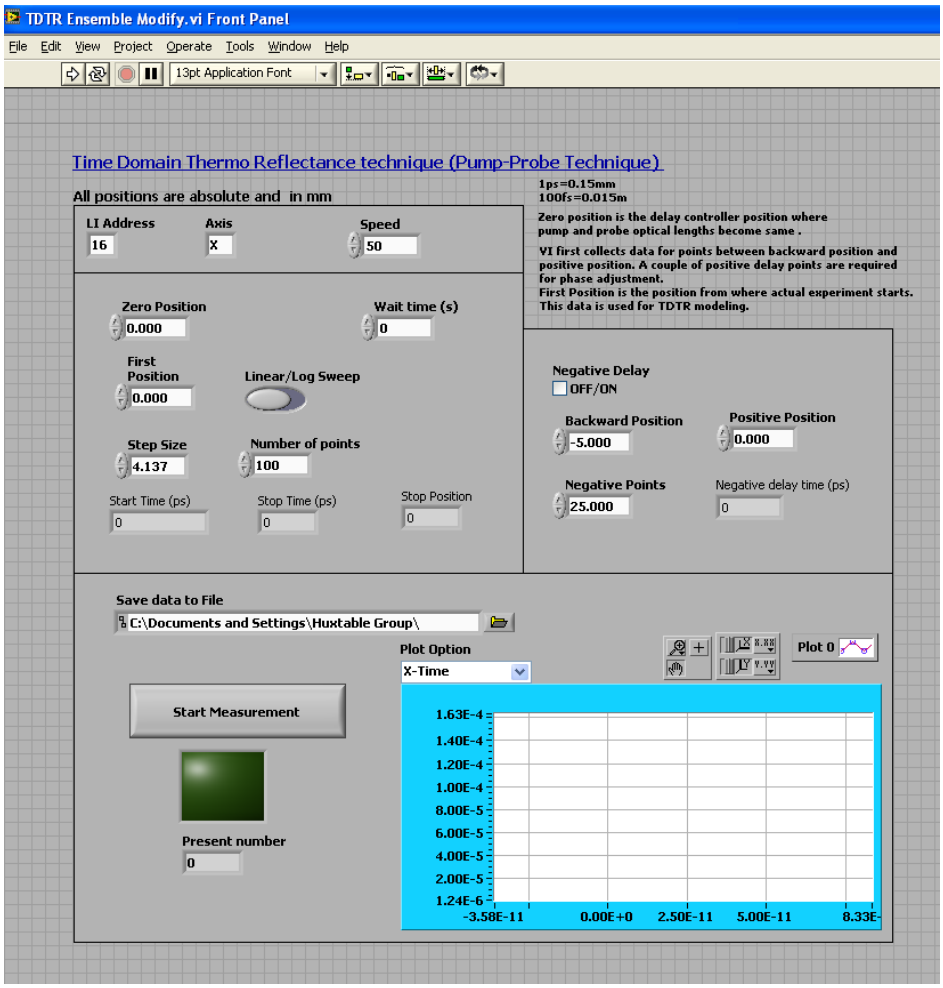

Figure 21: LabVIEW control panel and program created by Dr. Nitin Shukla. This program is used to acquire the raw data directly taken from the detector connected to the lock-in amplifier and used to mechanically control the delay stage. The raw data is saved in a spreadsheet.

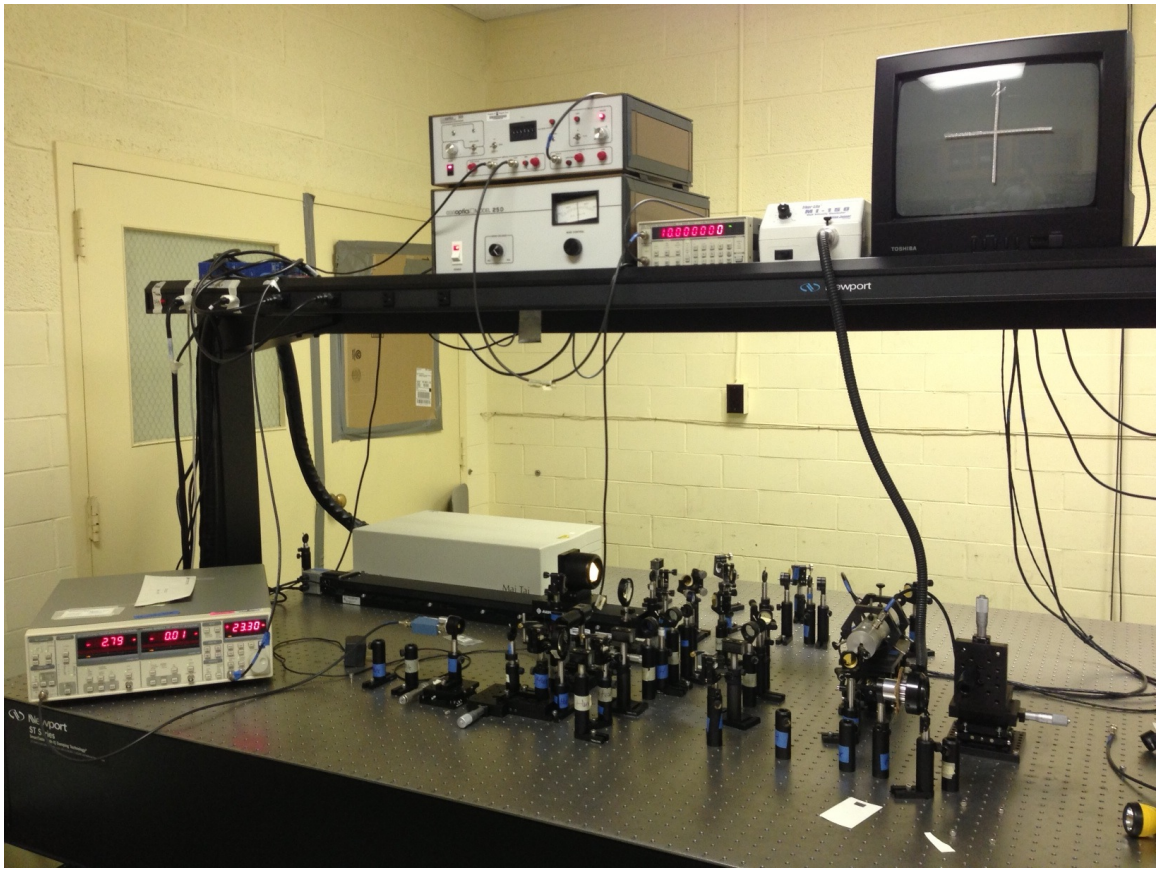

Figure 22: Current laser setup in the lab. The new titanium:sapphire femtosecond laser with a repetition rate ~ 80 MHz, and the wavelength tuning range is 690-1040 nm as shown in the small white box behind the delay stage. The lock-in amplifier is on the left-hand side of the optical table. On the bench top, from left to the right are: synchronous generator & power amplifier (from Conoptics Inc. model# 305 & 25D), function generator, lamp power and monitor for CCD camera.

The green color block represents the Agilent 34901A module as channel 1, and it connects to internal DMM that can measure both temperature and voltage. In order to have a precise measurement, there is a Keithley 2182A nano-voltmeter connected to it as an external DMM. The blue color block covers Agilent 34903A module as channel 2. The Agilent 34903A does not connect to internal DMM, and it only works as an on/off switch. The Agilent 34970A switch unit is very convenient for the combining use with the four-probe technique and other measurements.

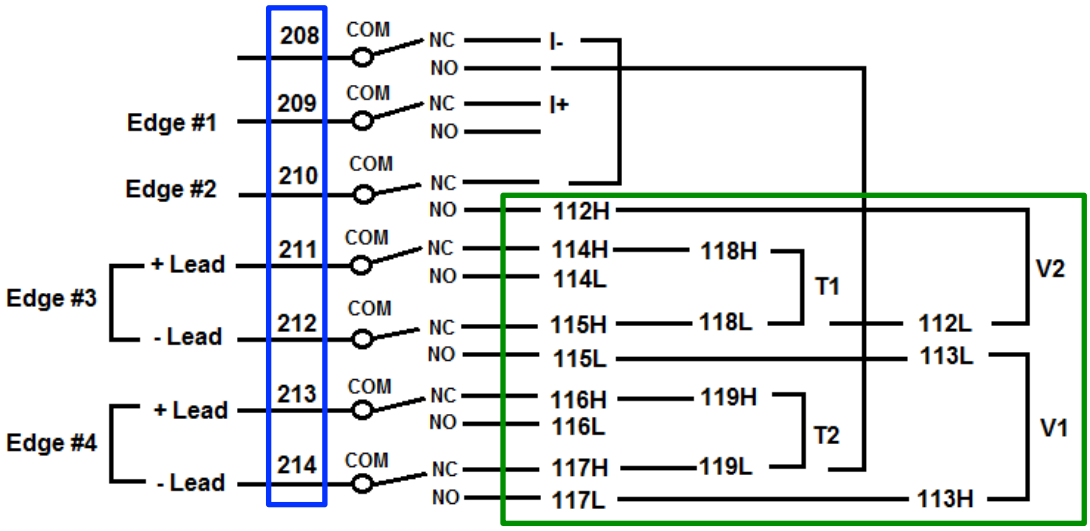

Figure 23: The connections among Keithley 6220 current supply, Aglient 34970 switch unit and Keithley nano-voltmeter. There are two modules: Agilent 34901A and 34903A modules used to complete this work. The Agilent 34901A module is in channel 1 (green color block), and it connects to internal DMM that can measure voltage and temperature that also connects to external current source and nano-voltmeter. The 34903A module is in channel 2 (blue color block), and this module does not connect to the internal DMM. This channel is only used to do switch job.

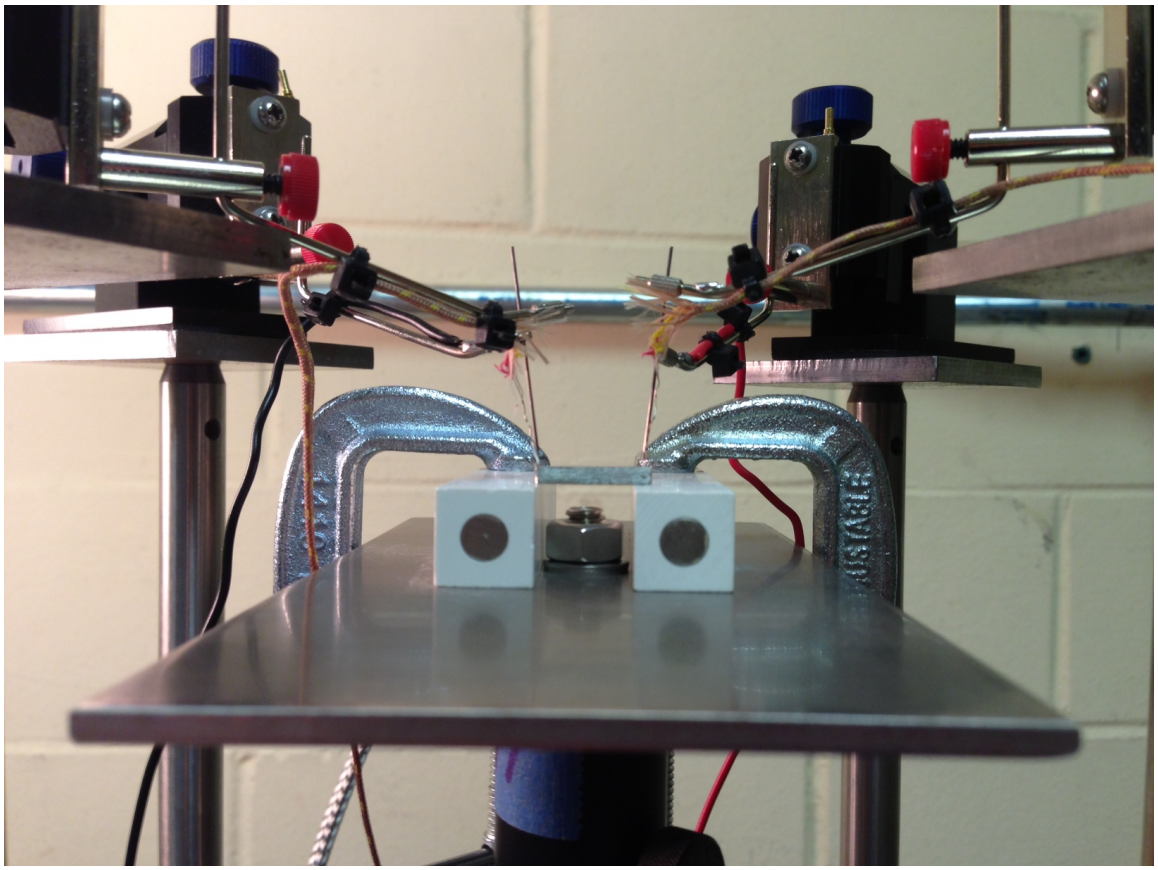

Figure 24: A side-view image taken from one of our testing sample, PbTe. The sample is the grey rectangular bar shown in the center of the image, while the white rectangles are the boron-nitride heat spreaders that contain the cylindrical cartridge heaters.

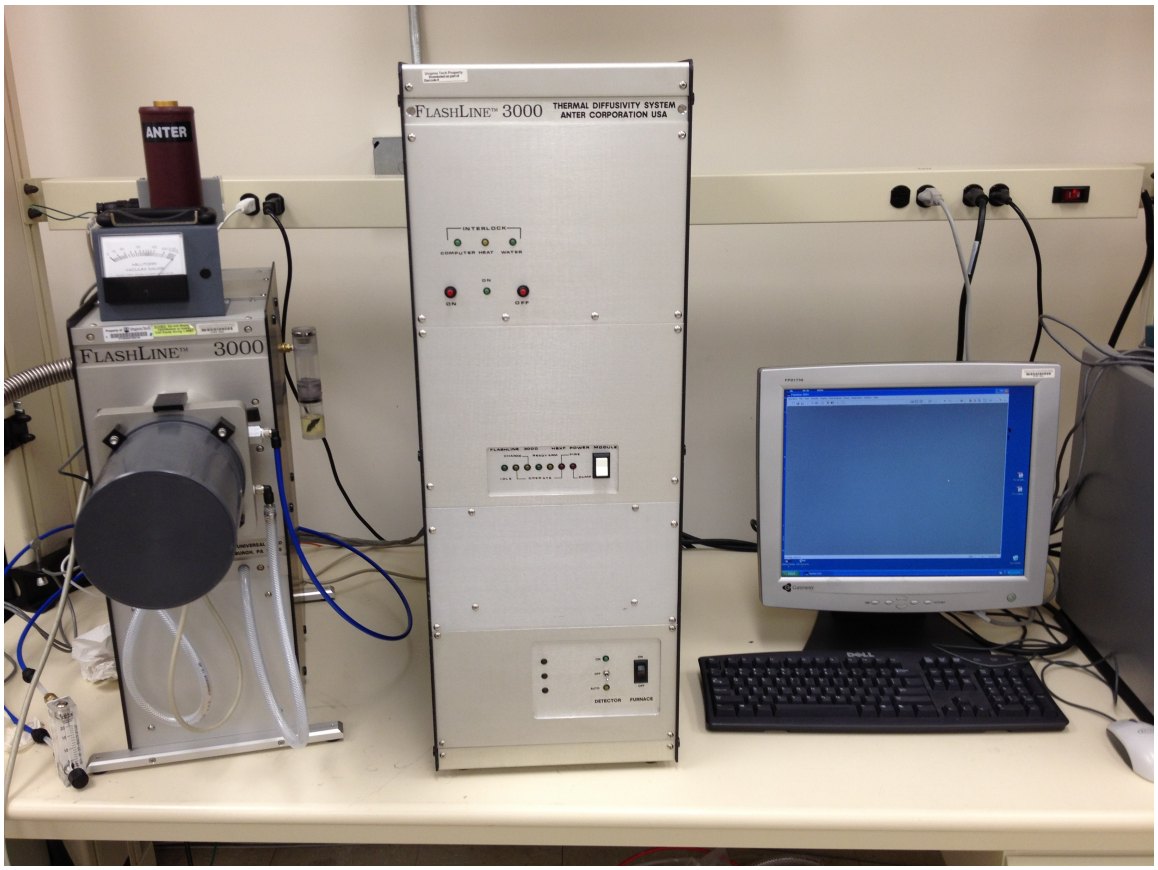

Figure 25: An apparatus of the Anter Flashline 3000 thermal diffusivity measuring system located in the center for power electronics system (CPES) at Virginia Tech. On the left hand side of is the furnace and sample holder (black cylinder chamber) On the top of it is the vacuum gauge meter. The center is the pulse source, power supply and control electronics. The computer is used for data acquisition.

Bibliography

1. V.P. Carey, G. Chen, C. Grigoropoulos, M. Kaviany, and A. Majumdar, "*A Review of Heat Transfer Physics,"* Nanoscale and Microscale Thermophysical Engineering, **12**(1): p. 1-60, 2008.
2. D.G. Cahill, W.K. Ford, K.E. Goodson, G.D. Mahan, A. Majumdar, H.J. Maris, R. Merlin, and S.R. Phillpot, "*Nanoscale Thermal Transport,"* Journal of Applied Physics, **93**(2): p. 793-818, 2003.
3. D.G. Cahill, K. Goodson, and A. Majumdar, "*Thermometry and Thermal Transport in Micro/Nanoscale Solid-State Devices and Structures,"* Journal of Heat Transfer-Transactions of the Asme, **124**(2): p. 223-241, 2002.
4. D.G. Cahill, "*Extremes of Heat Conduction-Pushing the Boundaries of the Thermal Conductivity of Materials,"* Mrs Bulletin, **37**(9): p. 855-863, 2012.
5. T.M. Tritt and M.A. Subramanian, "*Thermoelectric Materials, Phenomena, and Applications: A Bird's Eye View,"* Mrs Bulletin, **31**(3): p. 188-194, 2006.
6. L.E. Bell, "*Cooling, Heating, Generating Power, and Recovering Waste Heat with Thermoelectric Systems,"* Science, **321**(5895): p. 1457-1461, 2008.
7. T.M. Tritt, H. Boettner, and L. Chen, "*Thermoelectrics: Direct Solar Thermal Energy Conversion,"* Mrs Bulletin, **33**(4): p. 366-368, 2008.
8. J.P. Fleurial, "*Thermoelectric Power Generation Materials: Technology and Application Opportunities,"* Jom, **61**(4): p. 79-85, 2009.

9. M. Zebarjadi, K. Esfarjani, M.S. Dresselhaus, Z.F. Ren, and G. Chen, "*Perspectives on Thermoelectrics: From Fundamentals to Device Applications,"* Energy & Environmental Science, **5**(1): p. 5147-5162, 2012.

10. D.M. Rowe, *Thermoelectrics Handbook : Macro to Nano*. 2006, Boca Raton: CRC/Taylor & Francis.

11. A. Shakouri, *Recent Developments in Semiconductor Thermoelectric Physics and Materials*, in *Annual Review of Materials Research, Vol 41*, D.R. Clarke and P. Fratzl, Editors. 2011, Annual Reviews: Palo Alto. p. 399-431.

12. J.H. Yang and T. Caillat, "*Thermoelectric Materials for Space and Automotive Power Generation,"* Mrs Bulletin, **31**(3): p. 224-229, 2006.

13. J.H. Yang and F.R. Stabler, "*Automotive Applications of Thermoelectric Materials,"* Journal of Electronic Materials, **38**(7): p. 1245-1251, 2009.

14. C.T. Hsu, D.J. Yao, K.J. Ye, and B. Yu, "*Renewable Energy of Waste Heat Recovery System for Automobiles,"* Journal of Renewable and Sustainable Energy, **2**(1): p. 12, 2010.

15. K. Yazawa and A. Shakouri, "*Cost-Effective Waste Heat Recovery Using Thermoelectric Systems,"* Journal of Materials Research, **27**(9): p. 1211-1217, 2012.

16. N.Q. Le, J.C. Duda, T.S. English, P.E. Hopkins, T.E. Beechem, and P.M. Norris, "*Strategies for Tuning Phonon Transport in Multilayered Structures Using a Mismatch-Based Particle Model,"* Journal of Applied Physics, **111**(8), Art.No. 084310, 2012.

17. J.L. Lan, Y.H. Lin, Y. Liu, S.L. Xu, and C.W. Nan, "*High Thermoelectric Performance of Nanostructured In2o3-Based Ceramics,"* Journal of the American Ceramic Society, **95**(8): p. 2465-2469, 2012.

18. M.G. Kanatzidis, "*Nanostructured Thermoelectrics: The New Paradigm?,"* Chemistry of Materials, **22**(3): p. 648-659, 2010.

19. R. Venkatasubramanian, E. Siivola, T. Colpitts, and B. O'Quinn, "*Thin-Film Thermoelectric Devices with High Room-Temperature Figures of Merit,"* Nature, **413**(6856): p. 597-602, 2001.

20. B.C. Sales, "*Thermoelectric Materials - Smaller Is Cooler,"* Science, **295**(5558): p. 1248-1249, 2002.

21. D.Y. Li, S.T. Huxtable, A.R. Abramson, and A. Majumdar, "*Thermal Transport in Nanostructured Solid-State Cooling Devices,"* Journal of Heat Transfer-Transactions of the Asme, **127**(1): p. 108-114, 2005.

22. M.S. Dresselhaus, G. Chen, M.Y. Tang, R.G. Yang, H. Lee, D.Z. Wang, Z.F. Ren, J.P. Fleurial, and P. Gogna, "*New Directions for Low-Dimensional Thermoelectric Materials,"* Advanced Materials, **19**(8): p. 1043-1053, 2007.

23. G.J. Snyder and E.S. Toberer, "*Complex Thermoelectric Materials,"* Nature Materials, **7**(2): p. 105-114, 2008.

24. B. Poudel, Q. Hao, Y. Ma, Y.C. Lan, A. Minnich, B. Yu, X.A. Yan, D.Z. Wang, A. Muto, D. Vashaee, X.Y. Chen, J.M. Liu, M.S. Dresselhaus, G. Chen, and Z.F. Ren, "*High-Thermoelectric Performance of Nanostructured Bismuth Antimony Telluride Bulk Alloys,"* Science, **320**(5876): p. 634-638, 2008.

25. J. Martin, G.S. Nolas, W. Zhang, and L. Chen, "*Pbte Nanocomposites Synthesized from Pbte Nanocrystals,"* Applied Physics Letters, **90**(22), Art.No. 222112, 2007.

26. G.J. Fan, L.F. Fu, H. Choo, P.K. Liaw, and N.D. Browning, "*Uniaxial Tensile Plastic Deformation and Grain Growth of Bulk Nanocrystalline Alloys,"* Acta Materialia, **54**(18): p. 4781-4792, 2006.

27. L. Li, T. Ungar, Y.D. Wang, J.R. Morris, G. Tichy, J. Lendvai, Y.L. Yang, Y. Ren, H. Choo, and P.K. Liaw, "*Microstructure Evolution During Cold Rolling in a Nanocrystalline Ni-Fe Alloy Determined by Synchrotron X-Ray Diffraction,"* Acta Materialia, **57**(17): p. 4988-5000, 2009.

28. C. Suryanarayana, "*Nanocrystalline Materials,"* International Materials Reviews, **40**(2): p. 41-64, 1995.

29. C. Suryanarayana and C.C. Koch, "*Nanocrystalline Materials - Current Research and Future Directions,"* Hyperfine Interactions, **130**(1-4): p. 5-44, 2000.

30. S. Cheng, Y.H. Zhao, Y.M. Wang, Y. Li, X.L. Wang, P.K. Liaw, and E.J. Lavernia, "*Structure Modulation Driven by Cyclic Deformation in Nanocrystalline Nife,"* Physical Review Letters, **104**(25): p. 255501, 2010.

31. W.H. Wang, C. Dong, and C.H. Shek, "*Bulk Metallic Glasses,"* Materials Science & Engineering R-Reports, **44**(2-3): p. 45-89, 2004.

32. H. Gleiter, "*Nanocrystalline Materials,"* Progress in Materials Science, **33**(4): p. 223-315, 1989.

33. B.S. Murty, M.K. Datta, and S.K. Pabi, "*Structure and Thermal Stability of Nanocrystalline Materials,"* Sadhana-Academy Proceedings in Engineering Sciences, **28**: p. 23-45, 2003.

34. *Website*: http://what-when-how.com/nanoscience-and-nanotechnology/nanocrystalline-materials-synthesis-and-properties-part-1-nanotechnology/.

35. U. Erb, "*Size Effects in Electroformed Nanomaterials,"* Key Engineering Materials, **444**: p. 163-188, 2010.

36. A.L. Ruoff, *Introduction to Materials Science*. 1972, Englewood Cliffs, N.J.,: Prentice-Hall. xix, 697 p.

37. R. Berman, *Thermal Conduction in Solids*. Oxford Studies in Physics. 1976, Oxford Eng.: Clarendon Press. xi, 193 p.

38. J.M. Ziman, *Electrons and Phonons; the Theory of Transport Phenomena in Solids*. The International Series of Monographs on Physics. 1960, Oxford,: Clarendon Press. 554 p.

39. C.L. Tien, A. Majumdar, and F.M. Gerner, *Microscale Energy Transport*. Series in Chemical and Mechanical Engineering. 1998, Washington, D.C.: Taylor & Francis. xiv, 395 p.

40. G. Chen, "*Size and Interface Effects on Thermal Conductivity of Superlattices and Periodic Thin-Film Structures,"* Journal of Heat Transfer-Transactions of the Asme, **119**(2): p. 220-229, 1997.

41. G. Chen and M. Neagu, "*Thermal Conductivity and Heat Transfer in Superlattices,"* Applied Physics Letters, **71**(19): p. 2761-2763, 1997.

42. S.M. Lee, D.G. Cahill, and R. Venkatasubramanian, "*Thermal Conductivity of Si-Ge Superlattices,"* Applied Physics Letters, **70**(22): p. 2957-2959, 1997.

43. C. Kittel, *Introduction to Solid State Physics*. 8th ed. 2005, Hoboken, NJ: Wiley. xix, 680 p.

44. L.D. Hicks and M.S. Dresselhaus, "*Effect of Quantum-Well Structures on the Thermoelectric Figure of Merit,"* Physical Review B, **47**(19): p. 12727-12731, 1993.

45. J. Baxter, Z.X. Bian, G. Chen, D. Danielson, M.S. Dresselhaus, A.G. Fedorov, T.S. Fisher, C.W. Jones, E. Maginn, U. Kortshagen, A. Manthiram, A. Nozik, D.R. Rolison, T. Sands, L. Shi, D. Sholl, and Y.Y. Wu, "*Nanoscale Design to Enable the Revolution in Renewable Energy,"* Energy & Environmental Science, **2**(6): p. 559-588, 2009.

46. A.J. Minnich, M.S. Dresselhaus, Z.F. Ren, and G. Chen, "*Bulk Nanostructured Thermoelectric Materials: Current Research and Future Prospects,"* Energy & Environmental Science, **2**(5): p. 466-479, 2009.

47. D.G. Cahill, "*Analysis of Heat Flow in Layered Structures for Time-Domain Thermoreflectance,"* Review of Scientific Instruments, **75**(12): p. 5119-5122, 2004.

48. D.G. Cahill, W.K. Ford, K.E. Goodson, G.D. Mahan, A. Majumdar, H.J. Maris, R. Merlin, and P. Sr, "*Nanoscale Thermal Transport,"* Journal of Applied Physics, **93**(2): p. 793-818, 2003.

49. S. Huxtable, D.G. Cahill, V. Fauconnier, J.O. White, and J.C. Zhao, "*Thermal Conductivity Imaging at Micrometre-Scale Resolution for Combinatorial Studies of Materials,"* Nature Materials, **3**(5): p. 298-301, 2004.

50. S. Huxtable, *Time-Domain Thermoreflectance Measurements for Thermal Property Characterization of Nanostructures*, in *Handbook of Instrumentation and Techniques for Semiconductor Nanostructure Characterization*, R. Haight, F.M. Ross, and J.B. Hannon, Editors. 2012, World Scientific Publishing Co. : Hackensack, NJ. p. 587-610.

51. Y. Wang, J. Park, Y.K. Koh, and D.G. Cahill, "*Thermoreflectance of Metal Transducers for Time-Domain Thermoreflectance,"* Journal of Applied Physics, **108**: p. 043507, 2010.

52. K.E. O'Hara, X.Y. Hu, and D.G. Cahill, "*Characterization of Nanostructured Metal Films by Picosecond Acoustics and Interferometry,"* Journal of Applied Physics, **90**(9): p. 4852-4858, 2001.

53. K. Kang, Y.K. Koh, C. Chiritescu, X. Zheng, and D.G. Cahill, "*Two-Tint Pump-Probe Measurements Using a Femtosecond Laser Oscillator and Sharp-Edged Optical Filters,"* Review of Scientific Instruments, **79**(11), 2008.

54. J.M. Khosrofian and B.A. Garetz, "*Measurement of a Gaussian Laser-Beam Diameter through the Direct Inversion of Knife-Edge Data,"* Appl Opt, **22**(21): p. 3406-3410, 1983.

55. H.S. Carslaw and J.C. Jaeger, *Conduction of Heat in Solids*. 1959, New York: Oxford University Press.

56. A. Feldman, "*Algorithm for Solutions of the Thermal Diffusion Equation in a Stratified Medium with a Modulated Heating Source,"* High Temperatures-High Pressures, **31**(3): p. 293-298, 1999.

57. A.J. Schmidt, X.Y. Chen, and G. Chen, "*Pulse Accumulation, Radial Heat Conduction, and Anisotropic Thermal Conductivity in Pump-Probe Transient Thermoreflectance,"* Review of Scientific Instruments, **79**(11): p. 114902, 2008.

58. Y.K. Koh and D.G. Cahill, "*Frequency Dependence of the Thermal Conductivity of Semiconductor Alloys,"* Physical Review B, **76**(7): p. 075207, 2007.

59. J. Ravichandran, J.T. Kardel, M.L. Scullin, J.H. Bahk, H. Heijmerikx, J.E. Bowers, and A. Majumdar, "*An Apparatus for Simultaneous Measurement of Electrical Conductivity and Thermopower of Thin Films in the Temperature Range of 300-750 K,"* Review of Scientific Instruments, **82**(1), Art.No. 015108, 2011.

60. L.J. van der Pauw, "*A Method of Measuring the Resistivity and Hall Effect on Lamellae of Arbitrary Shape,"* Philips Technical Review, **20**: p. 220-224, 1958.

61. D.K. Schroder, *Semiconductor Material and Device Characterization*. 2nd ed. 1998, New York: Wiley. xxiv, 760 p.

62. K.D. Maglic and N.D. Milosevic, "*Thermal Diffusivity Measurements of Thermographite,"* International Journal of Thermophysics, **25**(1): p. 237-247, 2004.

63. C. Kittel, *Introduction to Solid State Physics*. 8 ed. 2005: John Wiley & Sons, Inc.

64. A. Nitzan, "*Chemistry - Molecules Take the Heat,"* Science, **317**(5839): p. 759-760, 2007.

65. X. Zheng, D.G. Cahill, P. Krasnochtchekov, R.S. Averback, and J.C. Zhao, "*High-Throughput Thermal Conductivity Measurements of Nickel Solid Solutions*

and the Applicability of the Wiedemann-Franz Law," Acta Materialia, **55**(15): p. 5177-5185, 2007.

66. C.Y. Ho, M.W. Ackerman, K.Y. Wu, S.G. Oh, and T.N. Havill, "*Thermal-Conductivity of 10 Selected Binary Alloy Systems,"* Journal of Physical and Chemical Reference Data, **7**(3): p. 959-1177, 1978.

67. L. Li, T. Ungar, Y.D. Wang, G.J. Fan, Y.L. Yang, N. Jia, Y. Ren, G. Tichy, J. Lendvai, H. Choo, and P.K. Liaw, "*Simultaneous Reductions of Dislocation and Twin Densities with Grain Growth During Cold Rolling in a Nanocrystalline Ni-Fe Alloy,"* Scripta Materialia, **60**(5): p. 317-320, 2009.

68. H.Q. Li and F. Ebrahimi, "*Synthesis and Characterization of Electrodeposited Nanocrystalline Nickel-Iron Alloys,"* Materials Science and Engineering a-Structural Materials Properties Microstructure and Processing, **347**(1-2): p. 93-101, 2003.

69. M.J. Aus, B. Szpunar, U. Erb, A.M. Elsherik, G. Palumbo, and K.T. Aust, "*Electrical-Resistivity of Bulk Nanocrystalline Nickel,"* Journal of Applied Physics, **75**(7): p. 3632-3634, 1994.

70. A.F. Mayadas, J.F. Janak, and A. Gangulee, "*Resistivity of Permalloy Thin Films,"* Journal of Applied Physics, **45**(6): p. 2, 1974.

71. N. Stojanovic, D.H.S. Maithripala, J.M. Berg, and M. Holtz, "*Thermal Conductivity in Metallic Nanostructures at High Temperature: Electrons, Phonons, and the Wiedemann-Franz Law,"* Physical Review B, **82**(7), 2010.

72. S.M. Lee and D.G. Cahill, "*Heat Transport in Thin Dielectric Films,"* Journal of Applied Physics, **81**(6): p. 2590-2595, 1997.

73. D.G. Cahill, S.K. Watson, and R.O. Pohl, "*Lower Limit to the Thermal-Conductivity of Disordered Crystals,"* Physical Review B, **46**(10): p. 6131-6140, 1992.

74. B.C. Gundrum, D.G. Cahill, and R.S. Averback, "*Thermal Conductance of Metal-Metal Interfaces,"* Physical Review B, **72**(24): p. 245426, 2005.

75. R.B. Wilson and D.G. Cahill, "*Experimental Validation of the Interfacial Form of the Wiedemann-Franz Law,"* Physical Review Letters, **108**(25), Art.No. 255901, 2012.

76. S.T. Huxtable, D.G. Cahill, and L.M. Phinney, "*Thermal Contact Conductance of Adhered Microcantilevers,"* Journal of Applied Physics, **95**(4): p. 2102-2108, 2004.

77. M.P. Allen and D.J. Tildesley, *Computer Simulation of Liquids*. 1987, Oxford: Clarendon Press.

78. P.K. Schelling, S.R. Phillpot, and P. Keblinski, "*Comparison of Atomic-Level Simulation Methods for Computing Thermal Conductivity,"* Physical Review B, **65**(14): p. 144306, 2002.

79. G. Chen, "*Particularities of Heat Conduction in Nanostructures,"* Journal of Nanoparticle Research, **2**(2): p. 199-204, 2000.

80. J. Chen, G. Zhang, and B.W. Li, "*How to Improve the Accuracy of Equilibrium Molecular Dynamics for Computation of Thermal Conductivity?,"* Physics Letters A, **374**(23): p. 2392-2396, 2010.

81. J.R. Lukes, D.Y. Li, X.G. Liang, and C.L. Tien, "*Molecular Dynamics Study of Solid Thin-Film Thermal Conductivity,"* Journal of Heat Transfer-Transactions of the Asme, **122**(3): p. 536-543, 2000.

82. A.J. Kulkarni and M. Zhou, "*Size-Dependent Thermal Conductivity of Zinc Oxide Nanobelts,"* Applied Physics Letters, **88**(14): p. 141921, 2006.

83. D.P. Sellan, E.S. Landry, J.E. Turney, A.J.H. McGaughey, and C.H. Amon, "*Size Effects in Molecular Dynamics Thermal Conductivity Predictions,"* Physical Review B, **81**(21): p. 214305, 2010.

84. Q.H. Tang, "*A Molecular Dynamics Simulation: The Effect of Finite Size on the Thermal Conductivity in a Single Crystal Silicon,"* Molecular Physics, **102**(18): p. 1959-1964, 2004.

85. G. Bonny, R.C. Pasianot, and L. Malerba, "*Fe-Ni Many-Body Potential for Metallurgical Applications,"* Modelling and Simulation in Materials Science and Engineering, **17**(2): p. 025010, 2009.

86. Y. Mishin, M.J. Mehl, and D.A. Papaconstantopoulos, "*Phase Stability in the Fe-Ni System: Investigation by First-Principles Calculations and Atomistic Simulations,"* Acta Materialia, **53**(15): p. 4029-4041, 2005.

87. S. Plimpton, "*Fast Parallel Algorithms for Short-Range Molecular Dynamics,"* Journal of Computational Physics, **117**(1): p. 1-19, 1995.

88. S. Murad and I.K. Puri, "*Thermal Transport through Superlattice Solid-Solid Interfaces,"* Applied Physics Letters, **95**(5): p. 051907, 2009.

89. W. Klement, R. Willens, and P. Duwez, "*Non-Crystalline Structure in Solidified Gold–Silicon Alloys,"* Nature, **187**: p. 869-870, 1960.

90. G.Y. Wang, P.K. Liaw, W.H. Peter, B. Yang, Y. Yokoyama, M.L. Benson, B.A. Green, M.J. Kirkham, S.A. White, T.A. Saleh, R.L. McDaniels, R.V. Steward, R.A. Buchanan, C.T. Liu, and C.R. Brooks, "*Fatigue Behavior of Bulk-Metallic Glasses,"* Intermetallics, **12**(7-9): p. 885-892, 2004.

91. M.B. Tang, H.Y. Bai, M.X. Pan, D.Q. Zhao, and W.H. Wang, "*Einstein Oscillator in Highly-Random-Packed Bulk Metallic Glass,"* Applied Physics Letters, **86**(2), Art.No. 021910, 2005.

92. M.B. Tang, H.Y. Bai, and W.H. Wang, "*Tunneling States and Localized Mode in Binary Bulk Metallic Glass,"* Physical Review B, **72**(1), 2005.

93. Z.H. Zhou, C. Uher, D.H. Xu, W.L. Johnson, W. Gannon, and M.C. Aronson, "*On the Existence of Einstein Oscillators and Thermal Conductivity in Bulk Metallic Glass,"* Applied Physics Letters, **89**(3), 2006.

94. M. Freels, G.Y. Wang, W. Zhang, P.K. Liaw, and A. Inoue, "*Cyclic Compression Behavior of a Cu-Zr-Al-Ag Bulk Metallic Glass,"* Intermetallics, **19**(8): p. 1174-1183, 2011.

95. D.C. Qiao, G.Y. Wang, P.K. Liaw, V. Ponnambalam, S.J. Poon, and G.J. Shiflet, "*Fatigue Behavior of an Fe48cr15mo14er2c15b6 Amorphous Steel,"* Journal of Materials Research, **22**(2): p. 544-550, 2007.

96. H.T. Grahn, H.J. Maris, and J. Tauc, "*Picosecond Ultrasonics,"* Ieee Journal of Quantum Electronics, **25**(12): p. 2562-2569, 1989.

97. D.R. Lide, *Crc Handbook of Chemistry and Physics*. 82nd ed. 2002, Boca Raton, FL: Chemical Rubber Company.

98. N.C. Shukla, H.H. Liao, J.T. Abiade, F.X. Liu, P.K. Liaw, and S.T. Huxtable, "*Thermal Conductivity and Interface Thermal Conductance of Amorphous and Crystalline Zr47cu31al13ni9 Alloys with a Y2o3 Coating,"* Applied Physics Letters, **94**(8), Art.No. 081912, 2009.

99. G.H. Zeng, J.H. Bahk, J.E. Bowers, H. Lu, A.C. Gossard, S.L. Singer, A. Majumdar, Z.X. Bian, M. Zebarjadi, and A. Shakouri, "*Thermoelectric Power Generator Module of 16x16 Bi(2)Te(3) and 0.6% Eras:(Ingaas)(1-X)(Inalas)(X) Segmented Elements,"* Applied Physics Letters, **95**(8), Art.No. 083503, 2009.

100. W. Kim, J. Zide, A. Gossard, D. Klenov, S. Stemmer, A. Shakouri, and A. Majumdar, "*Thermal Conductivity Reduction and Thermoelectric Figure of Merit Increase by Embedding Nanoparticles in Crystalline Semiconductors,"* Physical Review Letters, **96**(4), Art.No. 045901, 2006.

101. M. Yamasaki, S. Kagao, Y. Kawamura, and K. Yoshimura, "*Thermal Diffusivity and Conductivity of Supercooled Liquid in Zr41ti14cu12ni10be23 Metallic Glass,"* Applied Physics Letters, **84**(23): p. 4653-4655, 2004.

102. M. Yamasaki, S. Kagao, and Y. Kawamura, "*Thermal Diffusivity and Conductivity of Zr55al10ni5cu30 Bulk Metallic Glass,"* Scripta Materialia, **53**(1): p. 63-67, 2005.

103. N.C. Shukla, H.H. Liao, J.T. Abiade, M. Murayama, D. Kumar, and S.T. Huxtable, "*Thermal Transport in Composites of Self-Assembled Nickel Nanoparticles Embedded in Yttria Stabilized Zirconia,"* Applied Physics Letters, **94**(15): p. 151913, 2009.

104. N. Shukla, H.-H. Liao, L. Guido, and S. Huxtable. *Effect of Impurities on Thermal Conductivity of Gan*. in *American Society of Mechanical Engineers International Mechanical Engineering Congress and Exposition (ASME IMECE)*. 2009. Orlando, FL.